UCRL 8785

UNIVERSITY OF
CALIFORNIA
Ernest O. Lawrence
Radiation Laboratory

ANTIPROTON INTERACTIONS IN HYDROGEN AND CARBON BELOW 200 Mev

BERKELEY, CALIFORNIA

UCRL-8785
Physics and Mathematics
TID-4500 (15th Ed.)

UNIVERSITY OF CALIFORNIA

Lawrence Radiation Laboratory
Berkeley, California

Contract No. W-7405-eng-48

ANTIPROTON INTERACTIONS IN HYDROGEN AND CARBON BELOW 200 Mev

Lewis E. Agnew, Jr.
(Thesis)

July 23, 1959

Printed for the U. S. Atomic Energy Commission

Printed in USA. Price $2.50. Available from the
Office of Technical Services
U. S. Department of Commerce
Washington 25, D.C.

Contents

ANTIPROTON INTERACTIONS IN HYDROGEN AND CARBON BELOW 200 Mev

Lewis E. Agnew, Jr.

Lawrence Radiation Laboratory
University of California
Berkeley, California

July 23, 1959

ABSTRACT

About 500 antiprotons in a partially purified beam have been observed to enter the 30-in. propane bubble chamber. An arrangement of time-of-flight scintillation counters and a velocity-selecting counter enabled electronic identification of antiproton events, thus reducing scanning to a minimum and also providing a sample of antiprotons free of scanning bias. The antiprotons entered the propane at a kinetic energy of 220 Mev and were brought to rest. Scattering and annihilation interactions in both hydrogen and carbon have been observed vs. antiproton energy. Differential scattering cross sections have been obtained, and the following total cross sections have been measured for antiproton kinetic energies, T, in the ranges 75 to 137.5 Mev and 137.5 to 200 Mev:

Interaction	Cross section, σ (mb)	
	$75 \leq T \leq 137.5$	$137.5 \leq T \leq 200$
($\bar{p}p$) elastic	66 ± 17	56 ± 14
($\bar{p}p$) annihilation	112 ± 23	60 ± 18
($\bar{p}$-C) elastic (5° lab cutoff)	345 ± 60	255 ± 45
($\bar{p}$-C) annihilation	474 ± 76	360 ± 65

The above results show satisfactory agreement with the Ball-Chew theory where comparison can be made.

The details of the annihilation process in hydrogen and carbon have been observed. One feature of the experiment is that, in contrast to previous studies of annihilation products, we are able to make a direct observation of the neutral pions through pair production by π^0 decay photons. The significant results for carbon and hydrogen annihilations at an average antiproton kinetic energy of $\tilde{=}$ 100 Mev are:

	Hydrogen Annihilations		Carbon Annihilations	
Annihilation product	Multiplicity	Average total energy(Mev)	Multiplicity	Average total energy(Mev)
π^-	1.53 ± 0.08	402 ± 21	1.58 ± 0.07	366 ± 13
π^+	1.53 ± 0.08	379 ± 19	1.33 ± 0.08	371 ± 13
π^0	1.60 ± 0.50	356 ± 110	1.15 ± 0.30	342 ± 90

In addition to the above-listed annihilation products, the carbon stars contained nucleons that carried off more than 188 Mev per star. When pion absorption is considered, the carbon result of 4.1 ± 0.3 pions per annihilation is consistent with the observed hydrogen multiplicity of 4.7 ± 0.5 pions. Pion energy spectra and frequency distributions, as well as other details, have been obtained.

A total of 17 strange particles have been identified among the products of all the annihilations. This indicates that the production of a pair of K mesons occurs in 4.0 ± 1.2% of all annihilations. The average total energy per K pair is greater than 1200 Mev.

The charge-exchange process $\bar{p} + p \rightarrow \bar{n} + n$ has been observed and, based on six possible events, we obtain the inequality $\lambda \geqslant 630$ gm/cm^2 for the mean free path in propane ($50 \leqslant T_{\bar{p}} \leqslant 150$ Mev).

I. INTRODUCTION

Since the discovery of the antiproton by Chamberlain, Segrè, Wiegand, and Ypsilantis in 1955,[1] several counter and emulsion experiments have been performed in order to determine the interaction characteristics of the antiproton ($\bar{p}$).[2-9] In addition, a hydrogen-bubble-chamber experiment was recently performed.[10] A thorough review of the experimental and theoretical developments on antinucleons has been given recently by Segrè.[11]

Among the antiproton's interesting properties which have been observed are:

(a) Large cross sections for scattering and annihilation.

(b) Antiproton-nucleon annihilations near rest give an unexpectedly high multiplicity of about 5 pions.

(c) The production of K mesons in antiproton-nucleon annihilation is observed rarely.

(d) Little is known of the charge-exchange process ($\bar{p} + p \rightarrow \bar{n} + n$) by which the antineutron was detected electronically.

The 30-inch propane bubble chamber is well suited to the observation of the above phenomena. For instance, antiproton cross sections become difficult for counter techniques at low energies, while nuclear emulsions consist of a considerable variety of complex nuclei. But the propane bubble chamber allows observation of the very fundamental $\bar{p}p$ processes. An understanding of the low-energy (i.e. ~ 100 Mev) $\bar{p}p$ interaction is essential to any complete theory of nuclear forces. One theory has been proposed by Ball and Chew[12] which retains the structure of the nucleon-nucleon interaction suggested by Gartenhaus[13] and by Signell and Marshak,[14] with reasonable modifications to fit the nucleon-antinucleon case. Our results show support for the Ball-Chew theory on $\bar{p}p$ scattering and annihilation, within the validity of our statistics. It should be pointed out that a recent counter experiment,[9] as well as accumulated emulsion results,[15] also lend verification to the theory.

The annihilation process is especially adapted to bubble chamber observation. Not only may the charge of the annihilation products be determined, but momentum is also easily obtained. Furthermore, the large propane chamber enables the direct observation of π^0 annihilation products through pair production by the π^0 decay photons. Our result of 4.7 ± 0.5 pions per star is to be compared with the emulsion result[8] of 5.36 ± 0.3 and the hydrogen-bubble-chamber result[10] of 4.94 ± 0.31. In both the emulsion and hydrogen-bubble-chamber results, π^0 production is estimated through charge-independence arguments and energy considerations.

The natural attempt to explain the pion multiplicity by means of the Fermi statistical model has not been successful. Such high multiplicities as are observed seem to require a volume-of-interaction parameter Ω about 10 times the value expected when the Compton wave length of the pion is used as a radius. A different approach by Koba and Takeda,[16] wherein the pion cloud and nucleon core are treated separately, is more successful in predicting the high multiplicity observed.

Because we have analyzed more antiproton annihilations than all those previously reported, we have been able to establish a more confident estimate of the rate at which antiproton annihilations produce K-meson pairs. While observation of charged K mesons is often difficult, we have a high efficiency for detecting short-lived neutral strange particles. Our result that only 4.0 ± 1.2% of all annihilations yield a pair of K mesons is in disagreement with the various forms of the Fermi statistical model, which predict a higher ratio of K to π production. The low K multiplicity is in qualitative agreement with the Koba-Takeda model of the annihilation.

The charge-exchange process ($\bar{p} + p \rightarrow \bar{n} + n$), heretofore observed only electronically,[6,17] is especially adapted to bubble-chamber observation. However, charge exchange seems to be relatively infrequent compared to annihilation and elastic scattering, and the scope of our experiment permits little more than confirmation of the process.

II. APPARATUS AND METHOD

A. The Antiproton Beam

The primary object in the design of the beam is to maximize the number of antiprotons which can be observed in the bubble chamber. Satisfactory identification and analysis cannot be accomplished if the number of tracks in the central portion of the chamber is more than about 30. A momentum-analyzed beam of 700 Mev/c negative particles obtained directly from the Bevatron target at 6.1-Bev bombarding energy contains antiprotons in a ratio of about 1 in 500,000.[3] The undesired particles are mostly negative pions, with an estimated 5% of negative muons coming from π^- decays near the target (independent of additional π^- decay in the extracted beam), and probably an even larger percentage of electrons originating from conversions in the target of gamma rays that result from neutral-pion decays. In this experiment, the method of differential absorption was used to improve the ratio of antiprotons to undesired particles.

The method of differential absorption is based on the fact that for heavy charged particles the rate of momentum loss is given by[18]

$$-\frac{dP}{dx} = -\frac{1}{\beta c}\frac{dE}{dx} = \frac{4\pi e^4 z^2 NB}{mc^3\beta^3} \qquad (1)$$

with

$$B = Z\left[\ln\frac{2mc^2\beta^2}{I} - \ln(1-\beta^2) - \beta^2\right], \qquad (2)$$

where e and m are the electronic charge and mass, ze is the charge of the incident particle and βc is its velocity, N is the number of atoms of stopping material per unit volume, Z is the atomic number of the stopping material, and I is the mean excitation potential for an atom of the stopping material. It is seen that the momentum loss on passage through a block of material depends only on the β of the particle. Hence, if an analyzed beam of given initial momentum $P = m_j\gamma_j\beta_j c$ composed of several kinds of particles (j) is passed through an absorber, each kind of particle will emerge

with a different momentum and thus can be distinguished upon further momentum analysis. This method becomes ineffective at high momenta where all the β_j approach unity.

This method of making a separated beam is very simple. It requires only apparatus normally available at the Bevatron and was feasible before the construction of successful separators based on electrostatic deflection of particles.[9,19]

A layout of the beam apparatus is shown in Fig. 1. Table I gives descriptions of components of the apparatus. The 30-inch propane bubble chamber is described elsewhere.[20]

The 6.1-Bev circulating proton beam of the Berkeley Bevatron is directed upon a six inch long beryllium target (T in Fig. 1).[21] Negative particles produced at the target are deflected outward by the Bevatron's magnetic field and magnet M_1 so that only those of 970 Mev/c momentum can be delivered to a beryllium absorber at A_1.[22] Upon leaving A_1, the antiprotons have 848 Mev/c, while pions have 905 Mev/c. Deflection of the beam at M_2 causes a separation at A_2 based on the momentum difference between the two kinds of particles. This process of separation by differential absorption is then repeated, using the counters plus 9.4 g/cm^2 of beryllium as absorber at A_2 for the deflection at M_3. The antiproton beam has a momentum of 729 Mev/c upon leaving A_2, but only 684 Mev/c after passing through the chamber window and entering the propane. The three quadrupole-focusing magnets serve to maintain high beam intensity over the long channel. Except for the addition of a second separation, the beam is quite similar to that described by Chamberlain and others.[8]

Figure 2 gives beam-intensity profiles in the horizontal plane. Starting along the beam center line at the top and working downward, the first three curves give beam distributions for the direct beam (mostly pions) with no absorber. At A_1 the beam is horizontally dispersed in momentum and uniform in intensity as shown. The

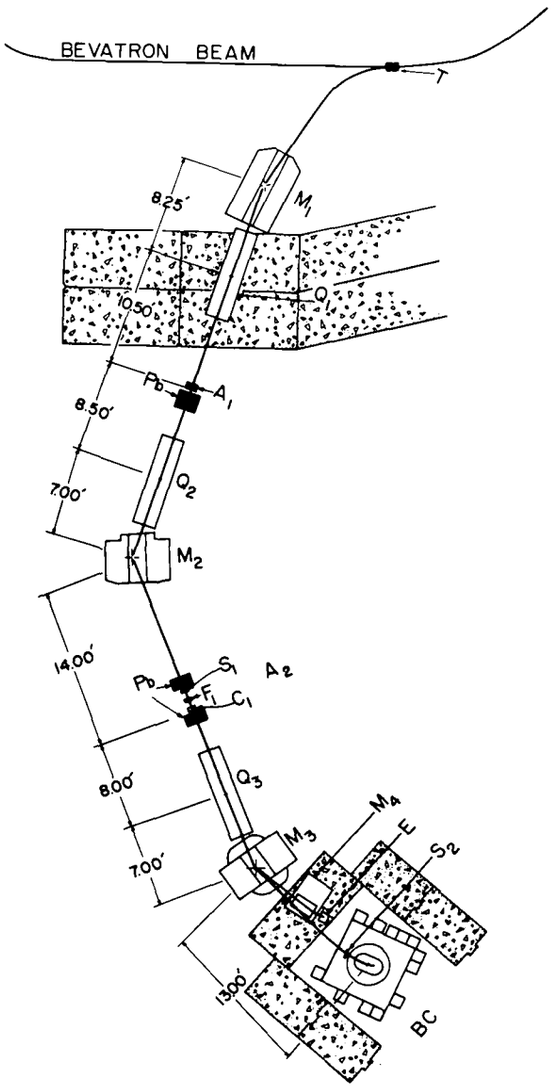

MUB-172

Fig. 1. Arrangement of apparatus to deliver antiprotons to the 30-inch propane bubble chamber. Brief descriptions will be found in Table 1. This apparatus was also used for the exposure of several emulsion stacks.

Table I

Components of the apparatus	
Symbol	Description
T	Bevatron target for production of antiprotons (beryllium, $\frac{1}{2}$ by $\frac{1}{2}$ by 6 in.)
M_1, M_2, M_3	Deflecting magnets: 15°, 40°, and 26° bending, respectively.
Q_1, Q_2, Q_3	Quadrupole focusing magnets of 8-in. aperture.
M_4	Deflecting magnet used in emulsion exposures.
E	Emulsion stack.
BC	Propane bubble chamber: 30 in. along the beam direction, 20 in. transverse to the beam, 6.5 in. deep, and filled with propane of density 0.42 g/cm^2.
A_1	Beryllium absorber: 32 g/cm^2 (for bubble chamber beam).
A_2	Absorber equivalent to 25 g/cm^2 of beryllium (for bubble chamber beam).
S_1	Plastic scintillation counter: $3\frac{1}{2}$ by $3\frac{1}{2}$ by $\frac{1}{2}$ in. thick.
C_1	Cherenkov counter, H_2O radiator, 4 by 4 by 2 in. thick.
F_1	Fitch-type Cherenkov counter: CS_2 radiator 4 in. diam by $2\frac{1}{4}$ in. thick.
S_2	Plastic scintillation counter: $7\frac{1}{4}$ by $2\frac{1}{2}$ by $\frac{1}{4}$ in. thick.
Pb	Lead collimators.

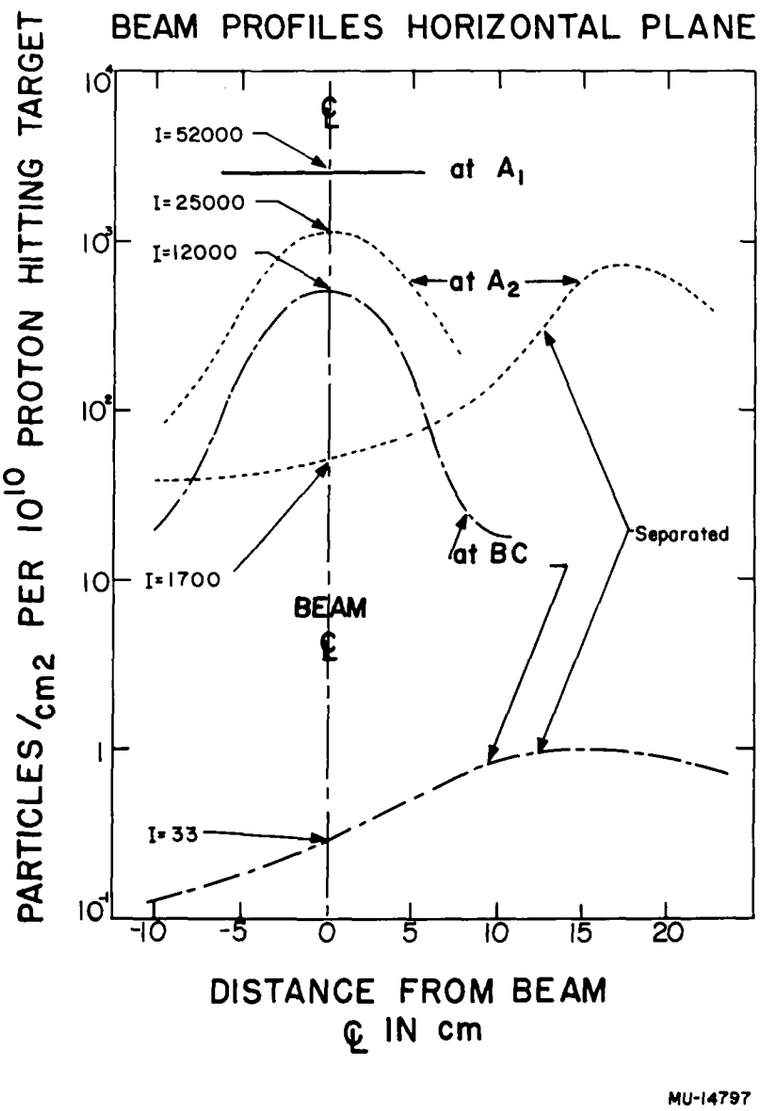

Fig. 2. Beam profiles in the horizontal plane with and without absorbers. Addition of absorber at A_1 and A_2 produces the displaced curves marked "separated" at A_2 and BC. To illustrate: At A_2 the direct beam has a peak on the beam center line of 1.2×10^3 particles/cm^2 per 10^{10} protons hitting the target and an integrated intensity of 25000 particles; after insertion of absorber at A_1, the peak at A_2 has shifted 17 cm and an integrated intensity of 1700 particles is found over the useful area at the beam center line.

quantity I = 52,000 indicates that 52,000 particles for each 10^{10} protons hitting the target were obtained by integrating over the useful beam area. It is seen that the beam is focused at A_2 and BC, and that transmission is imperfect even without absorbers, for only 25,000 particles per 10^{10} protons are delivered to the useful region at A_2, whereas 12,000 arrive at BC.

After addition of the absorber, the pion peak is displaced to the right looking along the beam and is less well focused (see curves labeled "separated" in Fig. 2). The intensity integrated over the useful area is drastically reduced, because the magnetic system is now tuned for antiprotons and the beam center line is located on the tail of the pion profile. About 33 particles per 10^{10} protons hitting the target arrive at the center of the bubble chamber. The contaminating particles at the bubble chamber are mostly muons which, even though displaced, can still enter the bubble chamber, as can be seen in Fig. 3.

The ratio of $\bar{p}$'s to undesired particles after the bubble chamber window is 67×10^{-6}. At the same momentum, the ratio of antiprotons to undesired particles at the target is about 1.6×10^{-6}. The purification factor is thus 42. For the entire experiment, the beam averaged about 2 antiprotons observed per hour of operation. Normal Bevatron beam level was 2×10^{10} protons per pulse at 600 pulses per hour.

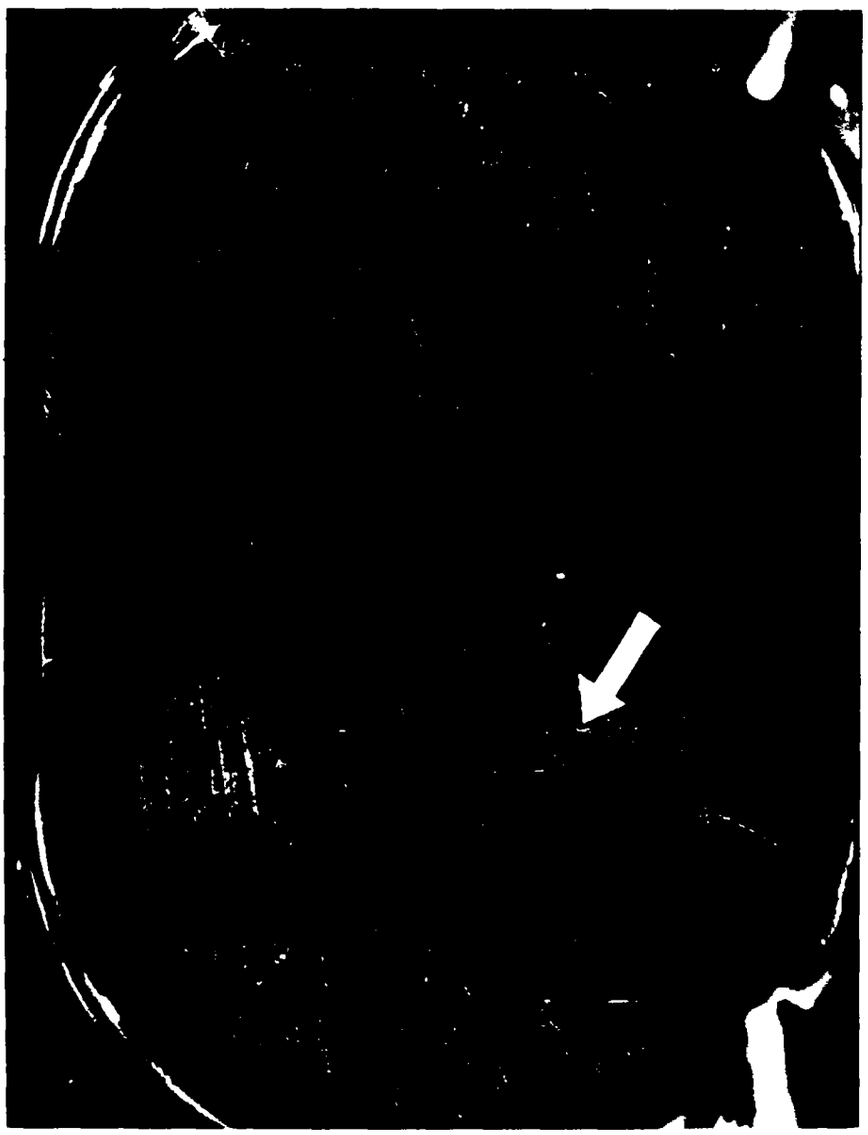

ZN-2201

Fig. 3. The 30-in. propane bubble chamber. This is a top view showing the undesired particles (87% μ^-, 10% π^-, 3% e^-) displaced to the left side of the chamber. An antiproton enters at top center and travels 50 cm without interaction before annihilating just below the center of the chamber.

B. Proton Calibration

By making minor changes in the operation of the apparatus, it was possible to extract a positive-proton beam. The protons were scattered from a copper target properly located with the Bevatron. The magnetic fields of all magnets were reversed to allow the transmission of positively charged beam, but the field magnitudes and all absorbers were kept identical to those used for antiprotons. The double momentum analysis (in M_2 and M_3) guaranteed the momenta to be the same within 2%. The proton beam was used to "calibrate" the chamber for antiprotons and to check the system of triggering counters.

The ranges of over 1000 protons entering the chamber were measured, and the distribution is shown in Fig. 4. It is seen that the incoming protons may be divided into two groups, a homogeneous group giving rise to a sharp peak and a smaller group having a continuous energy distribution downward from the maximum. Protons contributing to the sharp peak entered the bubble chamber window with a momentum distribution of 684 ± 20 Mev/c as determined by their range of 54 ± 5 cm. The short-range protons are due primarily to variations in wall thickness in the immediate vicinity of the window.

A photograph of a group of stopping protons in the chamber is seen in Fig. 5. Besides confirming the beam energy, studies of the position, ionization, and curvature of the stopping protons helped set up reliable criteria for antiproton identification.

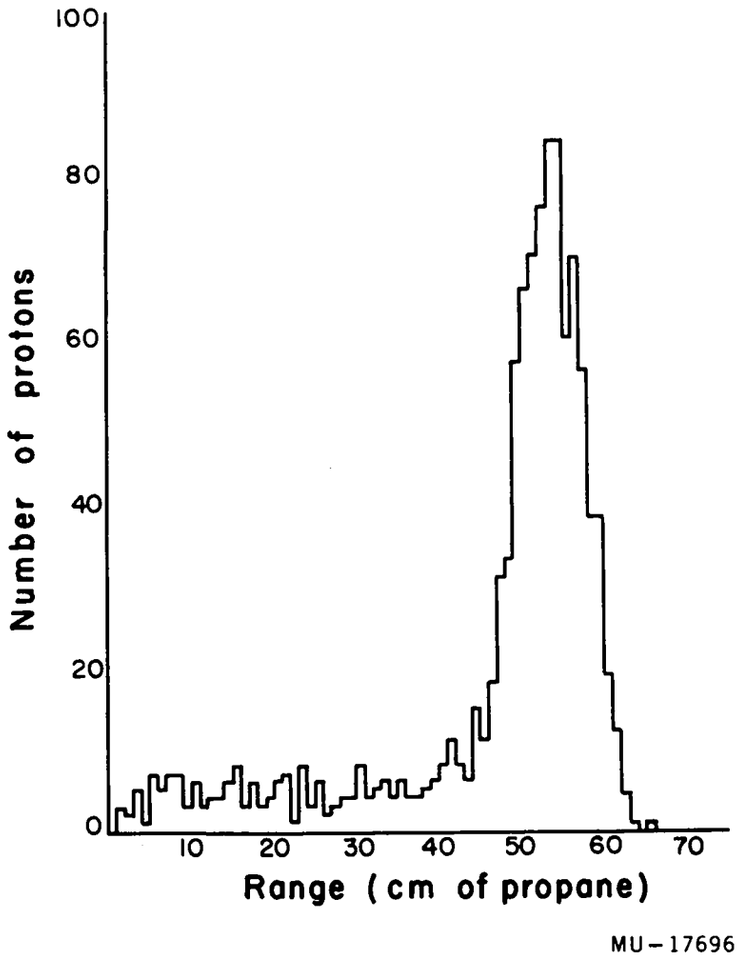

Fig. 4. The distribution in range of 1069 protons delivered to the bubble chamber through the same magnetic channel as the antiprotons.

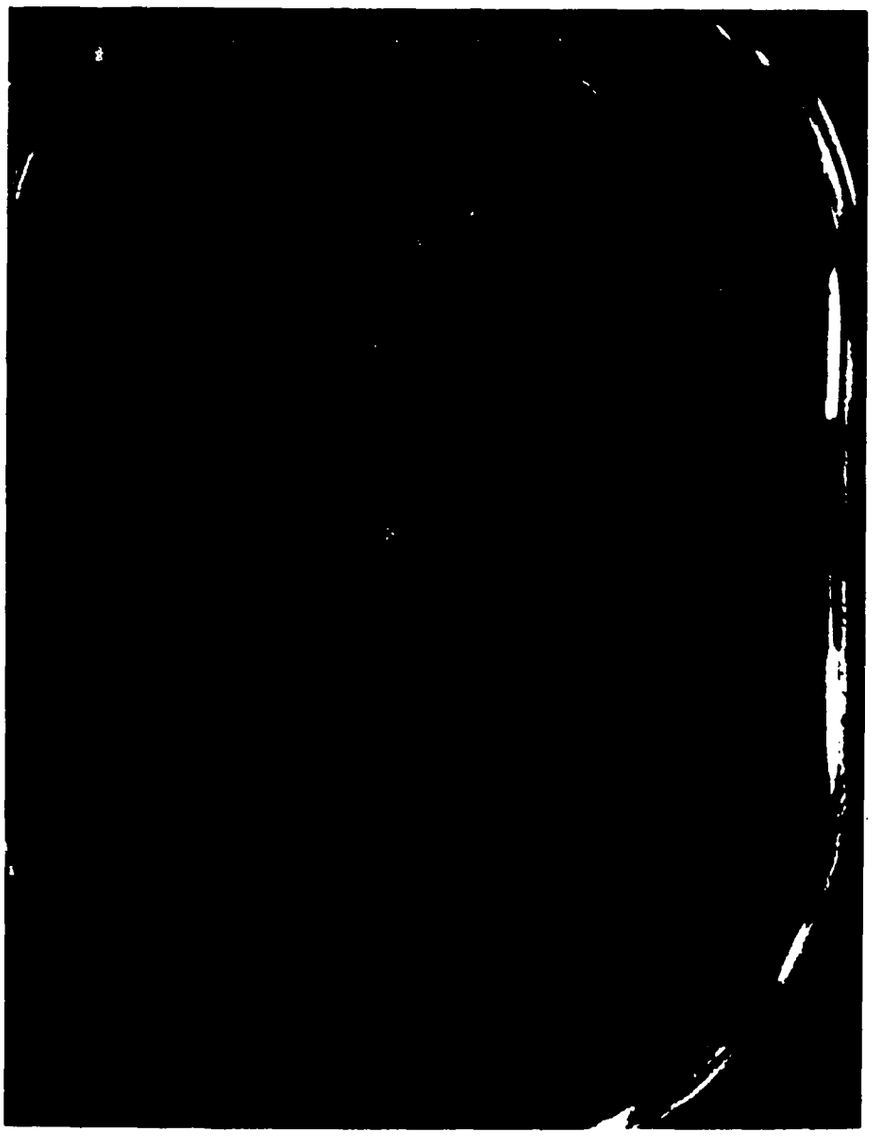

ZN-2200

Fig. 5. A typical bubble-chamber photograph of the stopping proton beam used to "calibrate" the antiprotons.

C. Electronic Selection of Antiprotons

It was recognized in the planning stage of the experiment that the rate of antiprotons appearing in the bubble chamber would be a few per hour. This posed a serious scanning problem, for there are 600 Bevatron beam pulses per hour. Not only would finding the antiprotons be a tedious job, but also it seemed evident that scanning might be biased toward those events that were most easily discovered by virtue of a many-pronged annihilation. These two difficulties were in great measure avoided through the use of a system of counters which selected those beam pulses for which the probability of an antiproton was high. In typical operation, the bubble chamber expansion is initiated with each Bevatron pulse about 45 msec before the beam arrives, and the lights are flashed some 6 msec after a 2-msec beam pulse passes through. This delay of the lights, which is necessary for proper bubble growth, is sufficient to allow the lights to flash only upon a command from the counters.

The counters are shown in Fig. 1 and briefly described in Table I. The two scintillation counters S_1 and S_2 are spaced 25 ft apart and define a time-of-flight measurement. The Fitch-type Cherenkov counter, F_1, has a response to particles of velocity corresponding to $0.62 \lesssim \beta \lesssim 0.78$. The water Cherenkov counter, C_1, responds only to particles with $\beta > 0.75$. At F_1, antiprotons in the beam have a β of 0.67, while the mesons approach $\beta = 1$. The requirements for an antiproton to be detected are (1) proper time delay between signals from S_1 and S_2; (2) a signal appears in F_1; and (3) no signal appears in C_1.

Bubble-chamber pictures were taken upon receipt of a signal triggered by proper coincidence of signals from S_1, S_2, and F_1. In order to guarantee photographing all antiproton events, the sensitivity of the trigger was adjusted so that more pictures were taken than just those that contained antiprotons. Signals from all four counters were displayed on an oscilloscope and photographed on 35-mm film. A simple numbering device suitably cross-indexed the oscilloscope traces and the bubble-chamber film. Upon scanning the oscilloscope film it was possible to select about 4% of the bubble-chamber pictures as possibly containing antiprotons. In half of these cases, unhurried scanning yielded an antiproton event.

D. Scanning and Measuring

A complete double scan was made of all bubble-chamber pictures that were electronically predicted to contain an antiproton. Only physicists participated in the scanning.

Each picture electronically selected was scanned with only the first 20 cm (about 1/3 of the antiproton range) visible. This was accomplished by means of a simple mechanical shutter attached to a projection scanning table. An attempt was made to identify the antiprotons by their ionization of approximately twice minimum. This was a fairly successful method: some 65% of the antiprotons were identified in the first 20 cm of track by ionization alone. Half of the remainder were not identified by track alone because they made spectacular interactions within the first 20 cm. Others were not identified in the first 20 cm of track because of overlapping μ tracks or occasional poor illumination near the chamber entrance.

Electronic selection, by reducing the number of pictures, enables almost unlimited scanning time per picture. Those antiprotons that were not recognized in the first 1/3 of their range were found upon thorough search of the entire chamber. Final identification usually amounted to no more than a careful check of ionization near mid-chamber, where a value of ~ 4 times minimum is expected.

Upon locating an antiproton interaction, each scanner made bubble-count ionization estimates, as well as tentative identification, for every prong. Each scanner also gave his interpretation of the event and specified detailed measuring procedures. Upon completion of measurement, both scan reports were compared with each other and with the measured momentum for each track segment. Any serious discrepancy between particle momentum and observed ionization was resolved by rescanning and remeasuring.

All events were measured by tracing out each track on the 70-mm film (in both views) with a digitized microscope that punches track coordinates directly into IBM-650 data cards. An IBM program was then used to make a least-squares fit to a parabola

projected on the horizontal plane and a straight line in the vertical plane. The slope of the straight line and the chord-sagitta relationship of the curve are sufficient to specify momentum upon further IBM computing, once magnetic field values within the chamber are known.

Routine computations give the dip and azimuthal angles of each track measured in addition to the momentum. Errors are assigned to each measured quantity as a part of the program. Errors reflect not only the internal consistency of the measured points along each track, but also known physical effects. For example, multiple scattering puts an accuracy limit of ±10% on momentum measurements by track curvature even for energetic particles, while momenta determined by range are much more accurate. Typical errors on angular measurements vary from a few tenths of a degree to a few degrees. Absolute positions within the chamber can be measured within a few millimeters, while relative positions can be determined much more precisely.

III. RESULTS: ANTIPROTON CROSS SECTIONS

A. Antiproton Path Length and Kinetic Energy

At the conclusion of the scanning and measuring processes, the total antiproton path length in the propane was computed. All 471 identified antiprotons upon which complete measurements could be made were accepted, while 84 events which were immeasurable because of imperfect film were excluded. The actual determination of path length for each individual event is easily done; however it is a little more difficult to assign an energy to a specific point along the track. Annihilations in flight restrict the use of residual range, and curvature measurements on low-energy antiprotons become inaccurate because of multiple scattering. A positive proton beam which was passed through the same momentum-analysis apparatus (see page 14) was used to "calibrate" the beam, and the antiprotons were assumed to have the same energy distribution as the protons upon leaving the final counter S2. Marked differences in wall thickness at the window of the chamber cause a significant number (20%) of "short-range" protons.

Each antiproton was assigned a kinetic energy at its first major interaction on the basis of the peak of the proton range distribution in the chamber, unless it was deemed to be a "short-range" $\bar{p}$. These "short range" $\bar{p}$'s were detected by requiring (a) the ionization to be heavy; (b) the position of the particle to indicate that it came through wall rather than window; and (c) the curvature to indicate approximate agreement.

The path lengths are summarized in Table II.

Table II

Summary of $\bar{p}$ path lengths

$\bar{p}$ kinetic energy (Mev)	50 to 75	75 to 100	100 to 125	125 to 150	150 to 175	175 to 200
$\bar{p}$ path length (cm)	1424	2194	2534	2996	3653	3108
H (gm/cm^2)	107	166	191	226	276	234
C (gm/cm^2)	483	745	860	1017	1240	1055

B. Antiproton-proton Elastic Scattering

The antiproton-proton elastic scatter is detectable in the propane bubble chamber. A photograph of a typical event is shown in Fig. 6. Such events with prominent recoil protons are easily identified. However, small-angle or low-energy $\bar{p}p$ scatters are indistinguishable from the recoilless $\bar{p}$-C scattering. For this reason, it is necessary to set up a cutoff angle for $\bar{p}p$ scattering.

In establishing a cutoff angle we have adopted the criterion that the recoil proton must have a range of at least 1 mm, which is sufficient to distinguish the scatter from $\bar{p}$-C. A cutoff angle determined in this way is dependent upon antiproton energy. For the energy interval 75 to 137.5 Mev, a center-of-mass (c.m.) angle of 25° is an appropriate cutoff, while 20° (c.m.) is suitable for the interval 137.5 to 200 Mev.

The 471 antiprotons which contributed to our path length had 42 observed $\bar{p}p$ elastic scatters. Each event was measured and verified by use of the unique two-body kinematics. In calculating cross sections we have divided the data into the two energy intervals indicated in the preceding paragraph. Table III gives the results, which average to 62 ± 12 mb (good geometry) over the entire range from 75 to 200 Mev.

The optical-theorem relationship $\frac{d\sigma}{d\Omega}(0^\circ) \geq \left(\frac{\sigma_t k}{4\pi}\right)^2$ was used to make the correction to good geometry. The total cross section σ_t used to obtain $\frac{d\sigma}{d\Omega}(0^\circ)$ was estimated by using the cutoff cross sections and the annihilation cross sections presented in Table IV. We assumed that $\frac{d\sigma}{d\Omega}$ was constant from 0° to θ_c (to compensate for the missing $\left[\text{Re } f(0^\circ)\right]^2$) and corrected the cross section by integrating from 0° to θ_c. This correction, which amounts to almost 25% of the good-geometry result, agrees satisfactorily with that predicted by the theoretical angular distribution of Fulco,[23] who used the Ball-Chew model.[12]

The Ball-Chew theory of the nucleon-antinucleon interaction, which is apparently successful, is based on the Yukawa interaction with the addition of a spin-orbit term and an absorbing central core that accounts for annihilation. The theory has only been applied to moderate

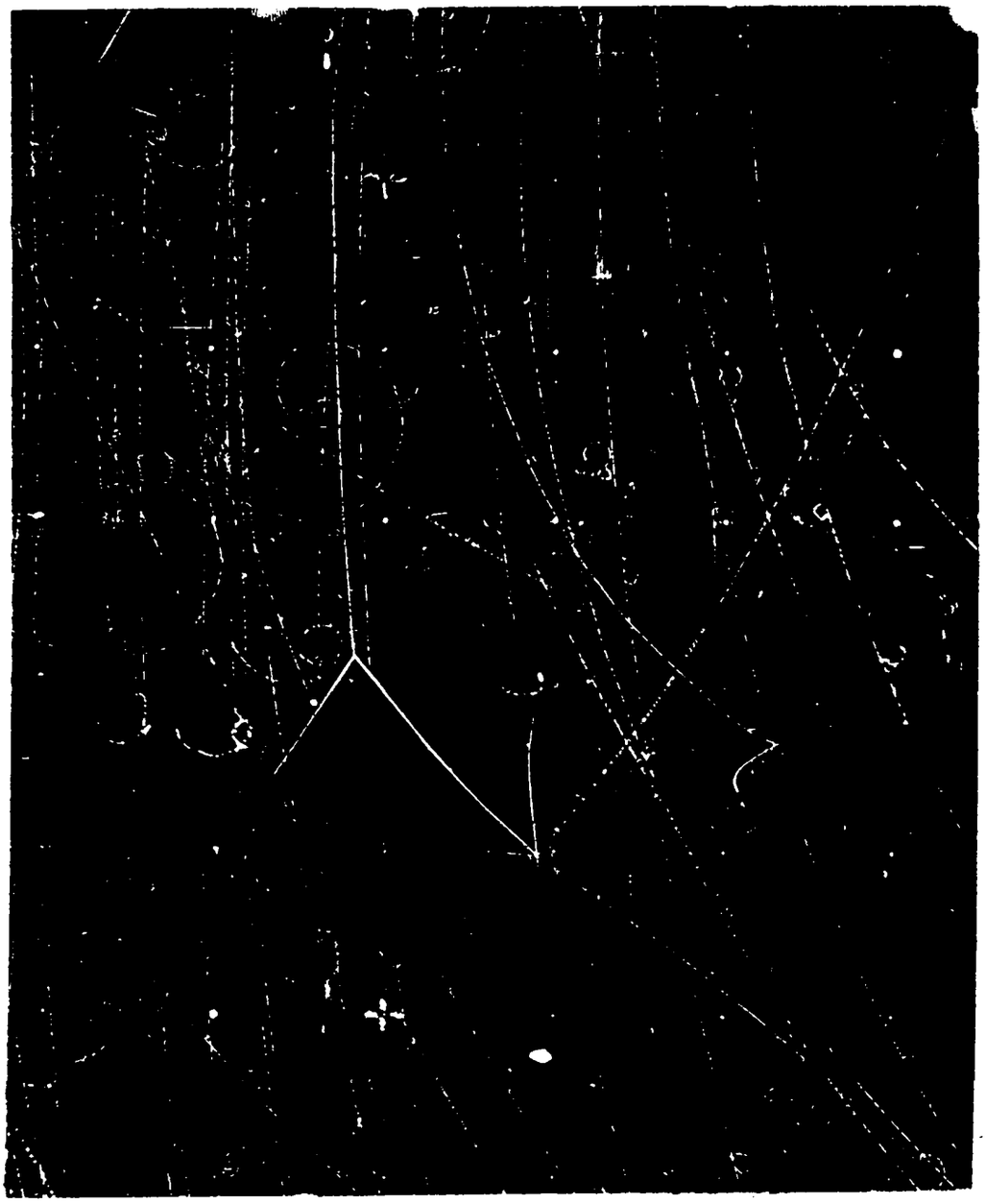

ZN-1929

Fig. 6. $\bar{p}p$ scattering. The antiproton (denser track) enters from the top to the left of center. At an energy of 117 Mev, the antiproton scatters 41° to its left from a proton. The recoil proton has a range of 4.4 cm (49 Mev). The scattered antiproton comes to rest in 8.3 cm (68 Mev) and annihilates on a carbon nucleus, showing 5 visible prongs.

Table III

$\bar{p}p$ elastic scattering[a]

$\bar{p}$ kinetic energy interval (Mev)	$75 \leq T_{\bar{p}} \leq 137.5$	$137.5 \leq T_{\bar{p}} \leq 200$
$\bar{p}p$ cutoff angle θ_c (c. m.)	25°	20°
$\sigma_{el}(\theta_c)$ millibarns	50 ± 13	46 ± 11
$\sigma_{el}(0^\circ)$ millibarns	66 ± 17	56 ± 14

[a] A large cutoff angle is adopted to safeguard against confusion with elastic scatters off carbon nuclei. The correction to $\sigma_{el}(0^\circ)$ is explained in the text.

energies. The original calculations were made at 140 Mev, where precise knowledge of the core radius is not crucial. At higher energies the details of the annihilation boundary condition become important. Below 50 Mev the WKB method of calculation breaks down. Ball and Fulco have extended the original calculations to 50 and 260 Mev.[24] Figure 7 compares their predictions with our results for $\bar{p}p$ reactions.

In Fig. 8, we present the angular distribution of the $\bar{p}p$ elastic scattering. Because of the small number of events (only 31 with scattering angle greater than $\theta_c = 25^\circ$), we have plotted one distribution for all antiproton energies from 75 to 200 Mev. The theoretical differential scattering cross section at 140 Mev given by Fulco[23] is also shown for comparison.

A summary of all $\bar{p}p$ elastic scatters reported to date in nuclear emulsions is presented in Table V.[25] Our results are in the same energy region and are included for comparison. By grouping together all the data from emulsions and the propane bubble chamber, we obtain an average value of $\sigma_{el} = 67 \pm 9$ mb at an average energy of about 137 Mev. This result is in good agreement with the Ball-Chew prediction of 73 mb at 140 Mev.

Table IV

Annihilation cross sections for antiprotons in hydrogen and carbon. Results are averaged over the energy ranges indicated.

Antiproton kinetic energy (T) in Mev	$75 \leqslant T \leqslant 137.5$	$137.5 \leqslant T \leqslant 200$
$\bar{p}p$ annihilation cross section	113 ± 23 mb	60 ± 18 mb
$\bar{p}$-C annihilation cross section	474 ± 76 mb	360 ± 65 mb

Table V

Summary of all $\bar{p}p$ data reported to date, excluding counter data

		Energy interval (Mev)	Path length (g/cm^2 of H)	Average energy (Mev)	$\sigma_{el}(\bar{p}p)$ (mb)
1.	Emulsions	30-250	726	140	73 ± 13
2.	Propane chamber	75-200	1093	135	62 ± 12
3.	1 and 2 combined		1819	137	67 ± 9
4.	Ball-Chew theory			140	73

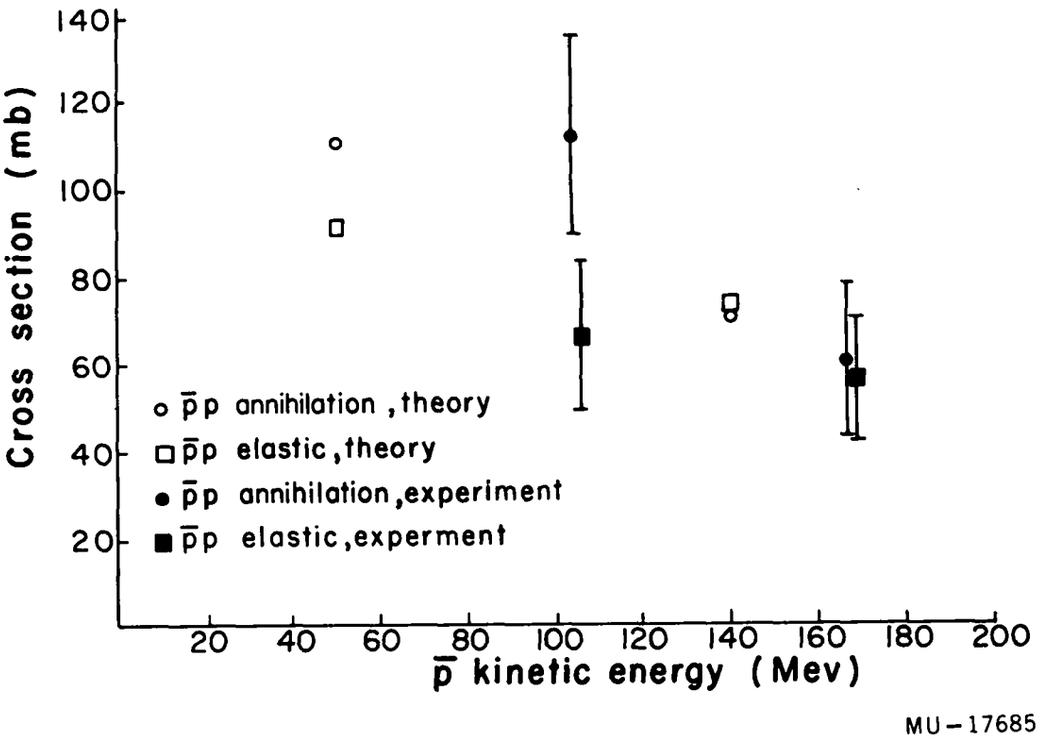

Fig. 7. $\bar{p}p$ cross sections. A comparison of theoretical (Ball-Chew model) and experimental $\bar{p}p$ elastic and annihilation cross sections. The experimental points are averages over two energy intervals, 75 to 137.5 Mev, and 137.5 to 200 Mev.

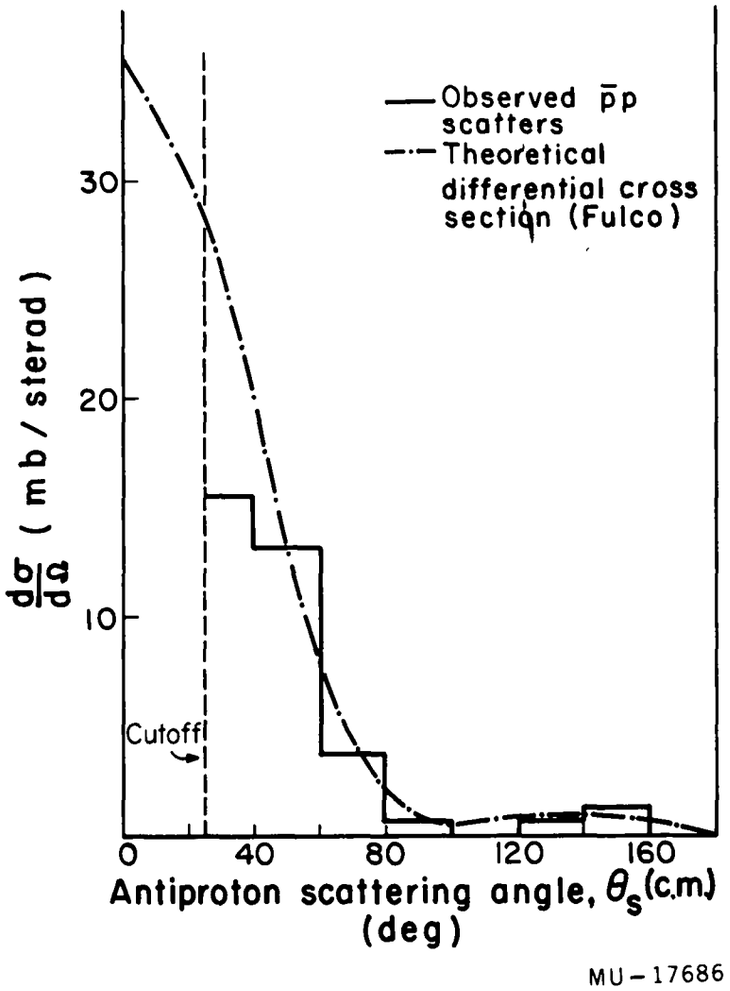

Fig. 8. Angular distribution for $\bar{p}p$ elastic scattering. Thirty-one events in 145 meters of antiproton track over an energy range from 75 Mev to 200 Mev are plotted. The cutoff angle is 25°(c.m.) The theoretical curve at 140 Mev by Fulco, based on the Ball-Chew model, is shown for comparison. Fulco predicts $\sigma_{el}(25)$ = 58 mb; our results are 47 ± 8 mb.

C. Antiproton-Carbon Elastic Scattering

An example of antiproton-carbon elastic scattering is shown in Fig. 9. Ordinary scanning and measuring techniques are adequate to treat $\bar{p}$-C elastic scatters except for small scattering angles, where scanning becomes very inefficient. For this reason we have established an angle of 3° projected upon the horizontal plane as a scanning limitation, thus we ignore those observed events with a smaller projected angle. A correction based on camera separation and height above the chamber, and on an assumed uniform distribution in ϕ of the $\bar{p}$-C scatters, is then applied to compensate for the missing events. This correction factor varies from 1.6 at a laboratory (lab) angle of 5° to 1.1 at 20° (lab). Another correction, which is smaller, is needed to remove $\bar{p}p$ elastic scatters that leave no recoil proton and hence are indistinguishable from $\bar{p}$-C elastic scatters.

We have adopted a cutoff angle of 5°(lab) for all $\bar{p}$-C elastic scattering events. This essentially eliminates the consideration of coulomb effects. An uncorrected total of 91 scatters of more than 5° was obtained in the antiproton energy region from 200 Mev to rest.

For the purpose of calculating elastic cross sections on carbon, most of the events fall into two groups: antiproton kinetic energies from 75 to 137.5 Mev, and from 137.5 to 200 Mev. Our results for θ (lab) $\geq 5^{\circ}$ are shown in Fig. 10. Also shown in Fig. 10 are the theoretical predictions of an optical-model calculation by Bjorklund and Fernbach using the nucleon-antinucleon phase shifts of Ball and Chew and the method of Riesenfeld and Watson to obtain the well-depth parameters.[24,26] This theory also predicts differential scattering cross sections for which calculations have been made at several energies. Our limited number of events does not warrant the presentation of more than one angular distribution including all events from 75 to 200 Mev, which is shown in Fig. 11. The theoretical differential cross section at 140 Mev is included for comparison.[26]

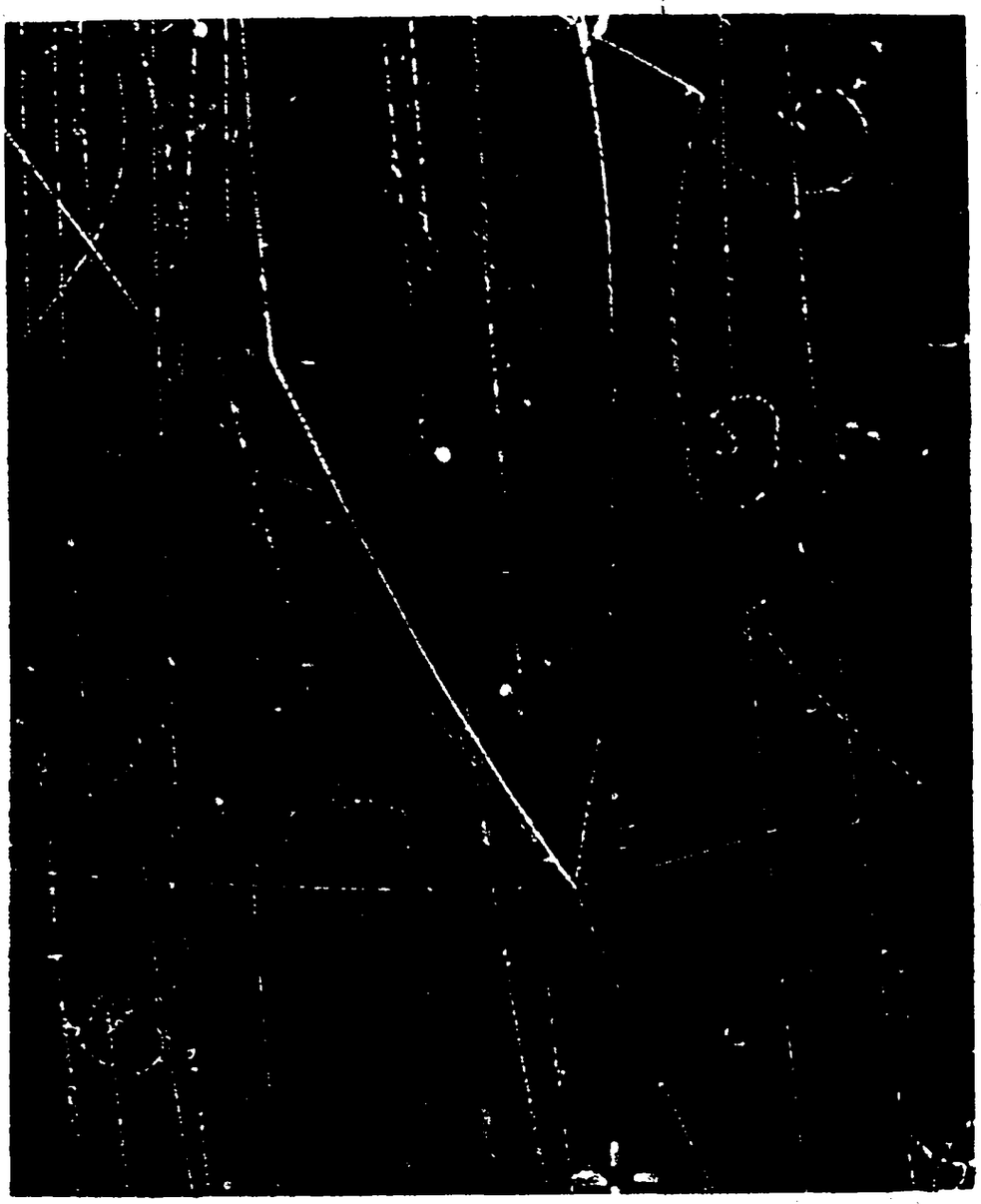

ZN-1934

Fig. 9. $\bar{p}$-C scattering. The antiproton (denser track) enters from the top and left of center. At an energy of ~65 Mev, the antiproton scatters 28° to its left and continues for 7.9 cm to the lower center of the picture, where it annihilates within a carbon nucleus. The visible products of the annihilation are three π^- and two π^+ mesons.

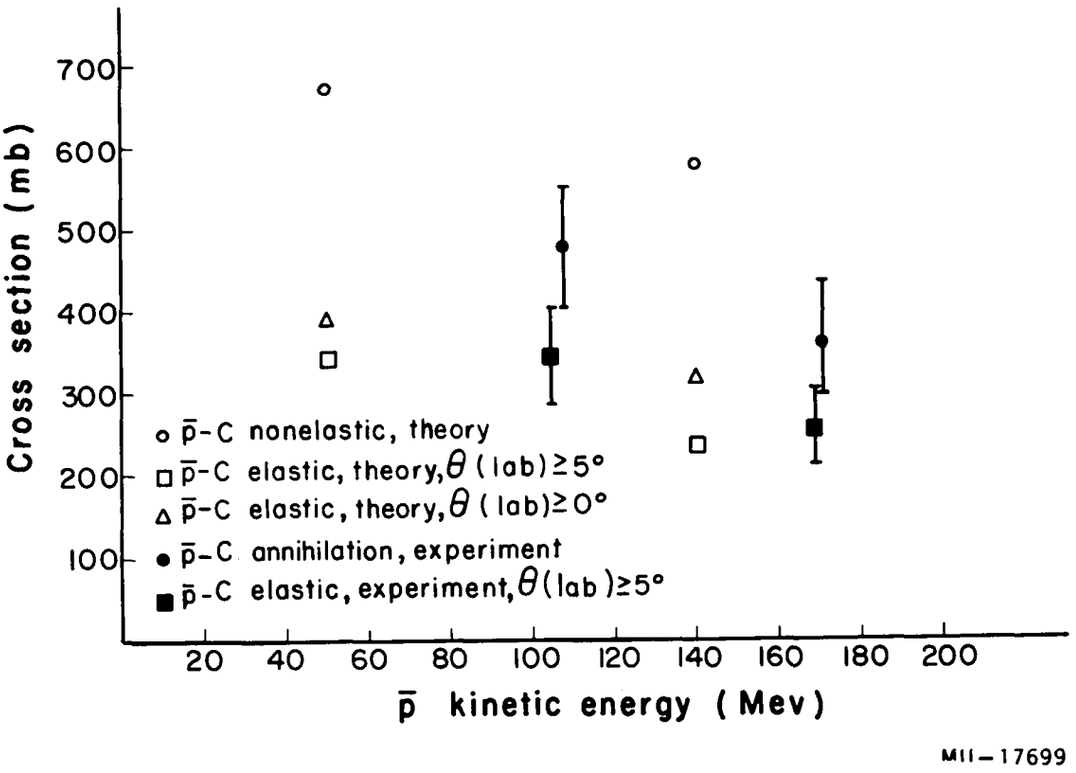

Fig. 10. $\bar{p}$-C cross sections. The experimental points are averages over two energy intervals, 75 to 137.5 Mev, and 137.5 to 200 Mev. The theoretical points are obtained by the use of Ball-Chew nucleon-antinucleon interaction in an optical-model calculation by Bjorklund and Fernbach. The theoretical values labeled nonelastic include charge-exchange and inelastic scattering as well as annihilation. Coulomb effects on elastic scattering are unimportant in the experimental points and are excluded in the theoretical points.

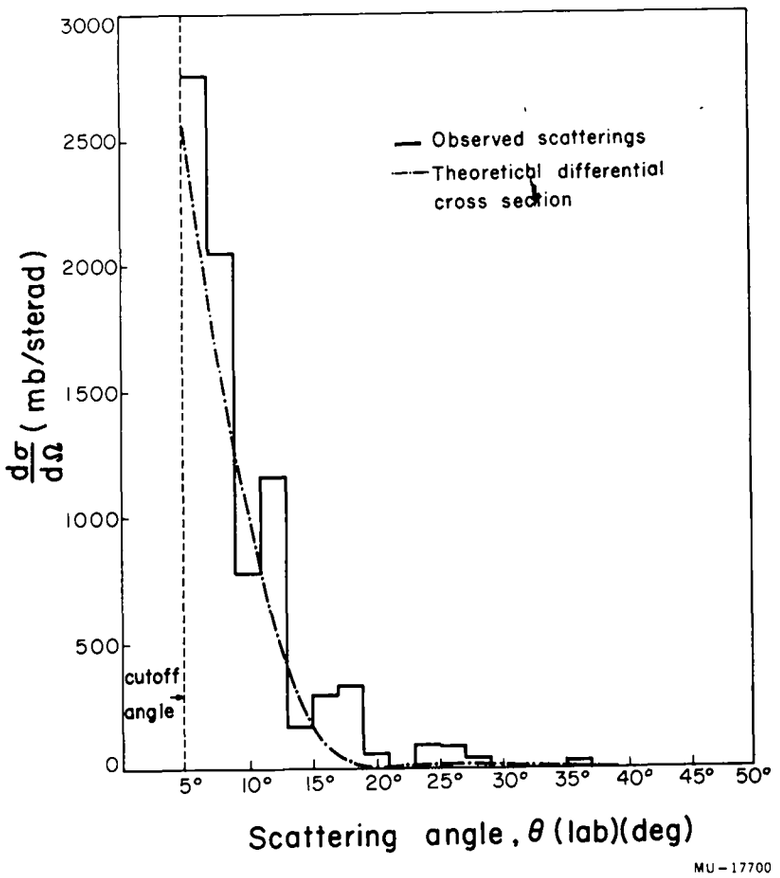

Fig. 11. $\bar{p}$-C differential scattering. This is a histogram showing our $\bar{p}$-C elastic-scattering differential cross section including all events of antiproton kinetic energy between 75 and 200 Mev. An optical-model curve due to Bjorklund and Fernbach, using the method of Watson and Riesenfeld and the Ball-Chew phase shifts for 140 Mev, is also shown.

D. Annihilation Cross Sections

Of the 471 antiprotons which contributed to our path length only 448 had tracks that terminated in the chamber, while the remainder scattered out at the top or bottom. Each annihilation was classified as having occurred in a carbon or hydrogen nucleus. Annihilations which result in an imbalance of charge or have nucleons among the products are obviously carbon stars. A hydrogen annihilation must have only pions (or K mesons) as products, and the net charge must be zero. All annihilations that fit these conditions were classified as hydrogen stars, although the conditions are not sufficient to fix the assignment. It is clear that an antiproton may annihilate within a carbon nucleus in such a way as to be indistinguishable from a hydrogen annihilation (e. g., in such a way as to "fake" a hydrogen annihilation), and a correction must be made for this effect before calculating annihilation cross sections.

Of our 448 terminating antiproton tracks, we were able to designate 302 annihilations as definitely carbon, and 146 as possibly hydrogen. Only 127 of the carbon annihilations were caused by antiprotons with more than 50-Mev kinetic energy, but 90 of the "possibly hydrogen" stars occurred in this manner.

In order to determine the annihilation cross sections, we must make corrections in the assignment of in-flight annihilations to hydrogen and carbon, i. e., corrections must be made for the fake $\bar{p}$-H stars mentioned earlier, and also for antiproton charge exchange.

The correction to account for charge exchange is necessary because the charge-exchange process simulates a $\bar{p}$-H annihilation into neutral pions. As pointed out in another section, we have estimated that 3 of the 11 detected ρ stars are really charge-exchange events, while the remaining 8 are possible hydrogen annihilations.

The correction to account for fake $\bar{p}$-H annihilation is determined by comparing the fake $\bar{p}$-H annihilation to a direct counterpart, the fake $\bar{p}$-neutron star, assuming they are equally probable. This is justified in the following two paragraphs.

The antiproton must annihilate on either a neutron or a proton within the carbon nucleus. The annihilation cross sections for $\bar{p}p$ and $\bar{p}n$ are predicted to be the same,[12] and there is experimental evidence that they are equal at a higher energy.[5] Since the carbon nucleus contains equal numbers of protons and neutrons, it seems likely that within the carbon nucleus an equal number of $\bar{p}p$ and $\bar{p}n$ annihilations take place.

If the pions emerge without interacting inside the carbon nucleus, then our assumption of equally probable fake $\bar{p}p$ and $\bar{p}n$ stars is justified. Moreover, if the pions do interact before leaving the carbon nucleus, it obviously suffices to consider for our argument here only pion interactions leading to the ejection of neutrons only. For such pion interactions, it is possible to show by I-spin arguments that the fake $\bar{p}p$ and $\bar{p}n$ annihilations are still almost equally probable.

Of the 40 annihilations which satisfied the conditions of a $\bar{p}n$ star, 15 occurred at $\bar{p}$ energies of more than 50 Mev. This means that we should expect that 15 of the in-flight hydrogen annihilations are really carbon, or in other words that 83% of the "possibly hydrogen" are indeed $\bar{p}$-H annihilations.

Table IV gives the annihilation cross sections on carbon and hydrogen after corrections. Average results are presented for two equal energy intervals from 75 Mev to 200 Mev, and are based on 54 hydrogen stars and 100 carbon stars. Statistical errors on both the "raw" numbers and the corrections were combined to yield the errors stated. These results agree qualitatively with the large absorption cross sections observed previously at various antiproton energies.[4, 5, 8, 9]

The Ball-Chew model, predicts $\bar{p}p$ annihilation cross sections of 110 mb at 50 Mev and 74 mb at 140 Mev.[24] Predictions of this model are compared with our experimental results in Fig. 7. While annihilation in the Ball-Chew model is not strongly dependent on core size, it is dependent in a cruder model suggested by Koba and Takeda.[16] There annihilation occurs upon an incoming antiproton of wavelength λ(c. m.) hitting an absorbing core of radius a to give $\sigma_{ann} = \pi(a + \lambda)^2$. For this model our results would suggest $a \cong 0.6\hbar/m_{\pi}c$.

IV. RESULTS: MISCELLANEOUS

A. Antiproton Charge Exchange and the ρ Star

The antiproton charge-exchange reaction $\bar{p} + p \rightarrow \bar{n} + n$ was used in the discovery of the antineutron[17] and in a later experiment.[6] Both of these experiments were counter experiments. A bubble chamber makes possible visual observation of both the charge-exchange process (disappearance of a $\bar{p}$) and the subsequent $\bar{n}$ annihilation (a neutral-produced star of large energy). Such an event has been observed in this experiment and is shown in Fig. 12. The antiproton track ends abruptly near mid-chamber. The angle between the antiproton direction and the line connecting the antiproton ending with the vertex of the star is 30° in the lab system. The visible energy release in the star is greater than 1500 Mev. The star is consistent with the process $\bar{n} + p \rightarrow 3\pi^{+} + 2\pi^{-} + \eta\pi^{0}$, where η is not greater than 2. The energy of the antiproton at the point of disappearance is estimated as 50 ± 30 Mev.

Unless antineutron annihilation occurs within the chamber, the charge-exchange process is difficult to distinguish from a $\bar{p}p$ annihilation in which all final-state pions are neutral (a "ρ star"). We have found eleven cases in which the antiproton track ends within the chamber with no star. Three of these cases have verified photon pair-conversions and thus must be considered ρ stars.[27] Two others occur at the end of the antiproton range and are also considered ρ stars, on the premise that charge exchange at very low energy will almost certainly lead to an $\bar{n}$ annihilation within the chamber. We are left with the following situation:

	Charge exchange	ρ stars	Undetermined
Number of events	1	5	5

The ρ star may be assumed to produce an average of at least 3.5 π^{0}. This number is obtained after observing that no annihilation has yet been reported in which all of the energy can be proven to appear in two charged pions.[28] According to conventional selection

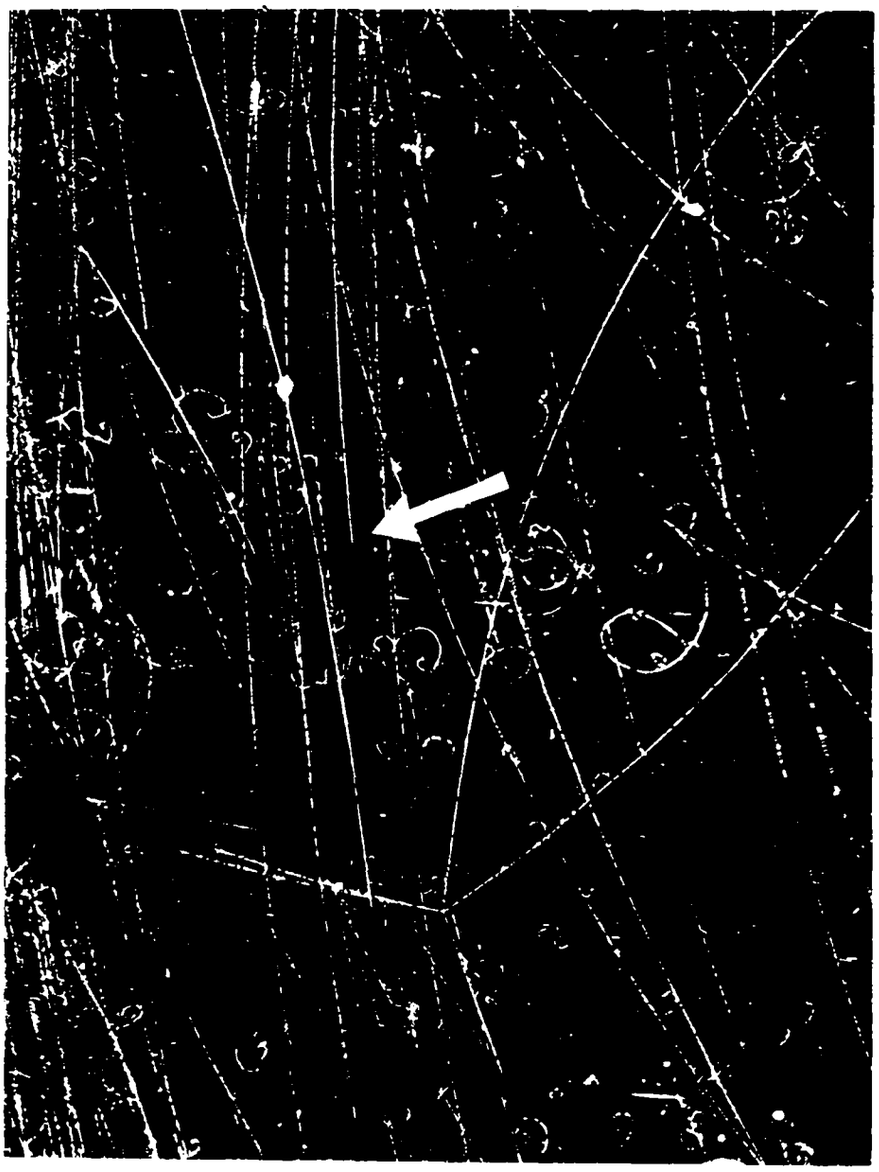

ZN-1930

Fig. 12. An antiproton charge exchange. The antiproton is incident from the top and to the left of center, and the antiproton ending is indicated by an arrow. The antineutron from the charge-exchange process annihilates in the lower center of the picture. Five charged pions are produced in the annihilation with an energy release $>$ 1500 Mev.

rules for two-pion annihilations, $\bar{p} + p \rightarrow \pi^+ + \pi^-$ should occur more often than $\bar{p} + p \rightarrow \pi^0 + \pi^0$.[29] Since the former is unobserved, the latter must be assumed to be rare also.

We may calculate the probability of recognizing a ρ star by observation of π^0 gamma conversions. The probability of seeing the event is $P = 1 - (1 - \epsilon)^{2\eta}$, where ϵ is the probability of detecting through pair production a gamma ray originating from a π^0, and η is the π^0 multiplicity. Since for this experiment $\bar{\epsilon} = 0.07$, we get $P \gtrsim 0.4$ for $\eta \gtrsim 3.5$.

At the risk of relying on extremely poor statistics, we may apply the probability $P = 0.4$ to the three events observed with pairs, to predict that 7.5 (i.e. 8) ρ stars actually occur. We may then assign 3 of the 5 undetermined events to be ρ stars, and 2 to be charge exchange, to get the following:

	Charge exchange	ρ star
Observed events	1	5
Assigned events	2	3
Total	3	8

We may make a check on the reasonableness of this division. It is possible that a maximum of 6 charge-exchange processes have been observed, if we eliminate the 5 "identified" ρ stars. The 6 candidates have an antiproton average kinetic energy of 88 Mev at the track ending. Their average position is slightly beyond mid-chamber. Assuming an isotropic center-of-mass differential cross section for charge exchange[24] and an $\bar{n}$ annihilation cross section equal to the estimated $\bar{p}$ cross section at 50 Mev, we calculate that 1/3 of the anti-neutrons produced should make a visible star. Thus the one $\bar{n}$ star we observe is consistent with our assignment of three events.

No really precise measurement of antiproton charge-exchange cross section has yet been made. The only previous report for energies below 200 Mev gives $\sigma(\bar{p} + p \rightarrow \bar{n} + n) = 10^{+2}_{-3}$ mb at 133 ±13 Mev in a

counter experiment.[9] Unfortunately, our bubble-chamber experiment permits little more than confirmation of the existence of the process. Because we are confident of our ability to identify antiprotons, especially at kinetic energies below 150 Mev, we are able to set an upper limit (with poor statistics) on the charge-exchange process. For the purposes of an upper limit, we will use the maximum of the possible charge-exchange events, namely six, rather than the estimated result of three events. For the mean free path for charge exchange in propane in the energy interval 50 to 150 Mev, we obtain $\lambda \geq 630$ gm/cm^2. This is consistent with charge-exchange cross-section limits $\sigma \leq 15$ mb for hydrogen (assuming all 6 events occurred on hydrogen), and $\sigma \leq 39$ mb for carbon (assuming all 6 events occurred on carbon).[31]

The Ball-Chew model predicts $\sigma(\bar{p} + p \rightarrow \bar{n} + n)$ to be 31 mb at 50 Mev and 21 mb at 140 Mev.[24]

B. Antiproton Interactions below 75 Mev

For antiproton kinetic energies below 75 Mev (10-cm range) it is impossible to determine energy accurately, because ionization rises above five times minimum, multiple scattering invalidates curvature measurements, and the distribution in range of stopping antiprotons has a full width of 10 cm. Nevertheless, it is possible to give some indication of low-energy interactions.

We obtained 16 antiproton-carbon elastic scatters at less than 75 Mev over a path length of approximately 2300 cm, yielding $\sigma_{el}(5^\circ) = 470 \pm 120$ mb after correction for scanning inefficiency. For the same energy interval, only 5 $\bar{p}p$ elastic scatters were detected above a 40° (c.m.) cutoff angle, yielding $\sigma_{el}(40^\circ \text{ c.m.}) = 48$ mb. If this result is corrected to good geometry by the use of the predicted differential scattering cross section of Ball and Fulco at 50 Mev,[24] we get $\sigma_{el}(\bar{p}p) \sim 77$ mb (5 events).

Annihilation cross sections at low energy are even more difficult to estimate than elastic events, for all the antiprotons must annihilate eventually. Direct comparison of the stopping proton distribution (Fig. 4) with the distribution of annihilations yields a rough

estimate of the cross sections from 0 to 75 Mev. These are $\sigma_{ann}(\bar{p}p)$ = 230 mb (24 events) and $\sigma_{ann}(\bar{p}\text{-}C)$ = 810 mb (32 events).

Upon coming to rest, an antiproton must be captured by either carbon or hydrogen, although the proportion captured by each is uncertain.[32] Antiproton capture by hydrogen produces the neutral system protonium, with an estimated principal quantum number of about n = 30. This estimate of the principal quantum number is based on the assumption that protonium is formed with a radius approximately that of the hydrogen atom. At larger distances, the charge of the proton is probably screened by an electron. The arguments that follow are all based on n = 30 for protonium, but the conclusions remain unchanged down to n = 15.

Protonium with n = 30 is a relatively stable system against radiative transition. Its transition probability (T. P.), if we consider all possible final states and assume that, in the initial state, the substates of the orbital quantum numbers ℓ are occupied according to their statistical weights, is T. P. = 1×10^{7} sec^{-1}. Even so, radiative transition is more probable than annihilation, as has been pointed out by Bethe and Hamilton,[33] except for S states, where annihilation can occur. For n = 30, the weight of the S state, again assuming population of the substates of ℓ according to their statistical weights, is much less than 1%. Thus protonium, as a neutral system nearly the size of the hydrogen atom having a thermal velocity of about 6×10^{5} cm/sec, lives long enough (except for the rare S-state annihilations) to make many collisions with hydrogen and carbon atoms in the propane.

According to a recent paper by Day, Snow, and Sucher,[34] the ℓ = 0 state of protonium (which annihilates) may become populated due to a Stark-effect process. This process should occur very quickly for all m = 0 states whenever the protonium is in a strong electric field. Such a strong field is encountered when the protonium system is within the Bohr radius of a proton. Protonium has about 21×10^{11} collisions per second with hydrogen atoms in propane. Because of the statistical weight of the m = 0 states, some 30 collisions are necessary to reduce

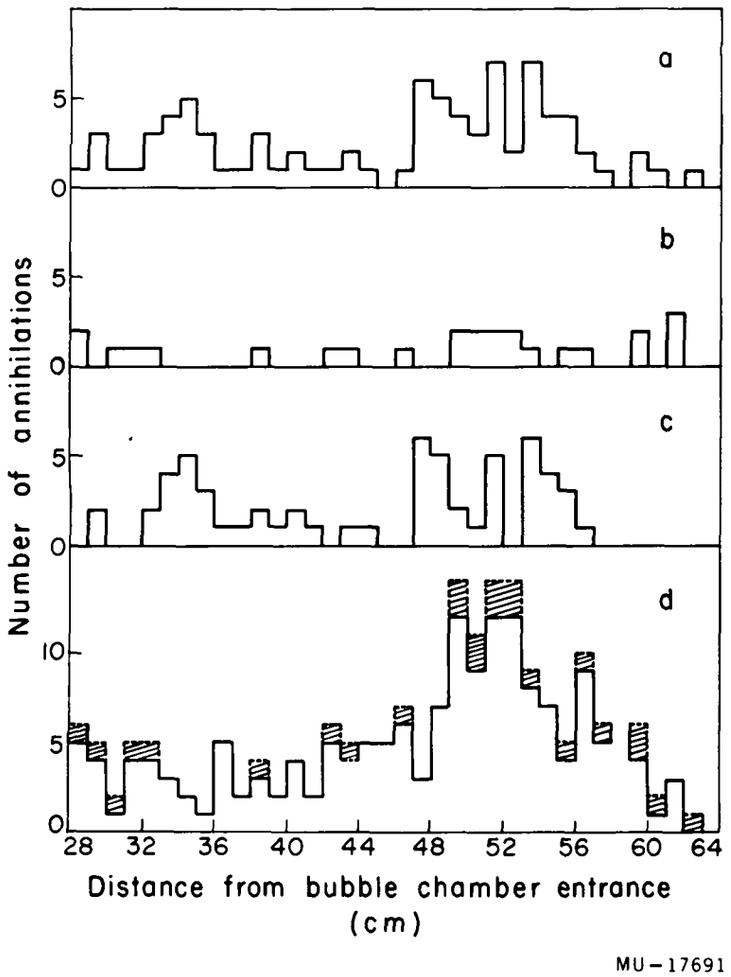

Fig. 13. Plots of the distribution, in distance from the bubble chamber entrance, of annihilation events that have suffered no previous interaction. (a) Apparent $\bar{p}$-H annihilations, (b) apparent $\bar{p}$n annihilations, (c) corrected $\bar{p}$-H annihilations (plot a minus plot b), (d) $\bar{p}$-C annihilations. Shaded blocks correspond to events removed from a to compensate for "fake" $\bar{p}$-H stars. The $\bar{p}$-C annihilations correspond to the sum of the shaded and unshaded areas.

the protonium by a factor of $1/e$, assuming that the m values are reshuffled on successive collisions. Thus we calculate that an approximate transition probability for protonium to annihilate (because of the Stark effect) is $(21 \times 10^{11})/30$, or about 0.7×10^{11} sec^{-1}.

Protonium annihilation is not as likely to result from collisions with carbon atoms. The protonium atom is several times as big as the unscreened region of the carbon atom, hence only the proton or the antiproton may be within that region at a given time. For such a situation another process becomes very likely. This is the transfer of the antiprotons to carbon, in an effect similar to that observed for stopping π^- mesons by Panofsky and others.[35] Protonium makes about 1×10^{11} collisions per second with the unscreened region of a carbon atom in propane, and for these collisions we assume that the transfer efficiency per collision is high. Ignoring any additional transfer due to not-so-close collisions with carbon, we have a rough lower limit of 1×10^{11} sec^{-1} for the transfer rate of antiprotons from protonium to carbon.

By comparing the rate of protonium annihilation (due to the Stark effect) to the rate of transfer of antiprotons from protonium to carbon, and remembering that many of the antiprotons are originally captured by carbon, we can see that annihilations on carbon should be most frequent for antiprotons at rest. Furthermore, the occurrence of $\bar{p}$-H annihilations in any perceptible number must be considered to be due to the Stark effect acting on protonium.

In Fig. 13 we have plotted the distribution within the chamber of $\bar{p}$-C annihilations, apparent $\bar{p}p$ annihilations, and apparent $\bar{p}n$ annihilations. If we assume that a fake $\bar{p}$-H annihilation occurs for each apparent $\bar{p}n$ star and substract b from a (Fig. 13), the result c which may be attributed to $\bar{p}p$ annihilations shows a less-prominent stopping distribution than for identifiable carbon annihilations. This suggests that the truly stopping antiprotons preferentially annihilate on carbon. To be more quantitative, we have found that for antiprotons of greater than 75 Mev, the ratio of carbon to hydrogen annihilations is about 2. For all annihilations at less than 50 Mev, the ratio becomes 6, and for 71 antiprotons of longest range, the ratio is 12. These values confirm the qualitative indication of Fig. 13.

Going a step farther than the apparent preference for annihilating on carbon, we may explore the assumption that such a highly efficient transfer mechanism exists that all annihilations of stopped antiprotons occur on carbon nuclei. Such an assumption forces us to attribute the end-of-the-range $\bar{p}p$ type annihilations to either (1) a sharp increase in the $\bar{p}p$ annihilation cross section at low kinetic energy, or (2) a significant preponderance of fake $\bar{p}p$ over fake $\bar{p}n$ stars. Consider Case 1: the assumption that $\bar{p}p$ annihilations at end-of-range really occur at low kinetic energies (which we can not distinguish from zero) leads to $\sigma_{ann}(\bar{p}p) = 455 \pm 105$ mb (0 to 75 Mev). Such a large cross section is unlikely in view of the 1/v law prediction of < 200 mb. Let us then reject Case 1 and consider Case 2, where we obtain a ratio of 1.8 ± 0.5 when comparing $\bar{p}p$-type carbon annihilations with $\bar{p}n$-type annihilations at rest. This ratio is not at all inconceivable, but it is not in good agreement with an expected ratio of 1.0.

We conclude that we have established that stopping antiprotons anninilate preferentially on carbon in propane, which is expected. It is even possible that the stopped antiprotons annihilate wholly on carbon, but this hypothesis leads to conclusions that are not entirely satisfactory. Indeed, our results are in best agreement with the annihilation of about 10% of all stopping antiprotons on hydrogen, which is reasonably explained by the Stark-effect process.

C. Antiproton Polarization

In the design of the experiment, the possibility that carbon might be a good analyzer was acknowledged, even though no mechanism for antiproton polarization in production has been suggested. Antiprotons of 970 Mev/c initial momentum observed here were produced on a beryllium target by 6.1-Bev protons. Their angle of production was 5° left (lab), which corresponds to 169° (c. m.). Any polarization at production is expected to survive energy degradation.

The optical-model potential of Riesenfeld and Watson[36] contains a spin-orbit term for which the theoretical phase shifts of the nucleon-antinucleon system of Ball and Chew enable a calculation of polarization in $\bar{p}$-C elastic scattering. This calculation has been made by Bjorklund and Fernbach,[37] who predict a uniformly increasing polarization from about 0.1 at 5°(lab) to about 0.3 at 20° for an antiproton kinetic energy of 140 Mev. The polarization increases with energy and does not appear to change sign over the region of interest. Thus we have theoretical reasons for believing the $\bar{p}$-C elastic scattering will provide an analysis of the antiproton beam.

The right-left asymmetry of the $\bar{p}$-C scatters within 45° of the horizontal plane was $e_{R-L} = 0.12 \pm 0.17$, while an up-down asymmetry of $e_{U-D} = 0.18 \pm 0.15$ was obtained. These results are consistent with zero polarization in antiproton production. We cannot determine whether this negative result is due to a real absence of polarization in the antiproton beam, or whether it is due to the lack of analyzing power in carbon scattering (the analyzability is theoretically estimated to be only about 0.2).

V. RESULTS: THE ANNIHILATION PROCESS

A. Observation of Annihilation Products

Reports published previously have described the annihilation process in nuclear emulsions[7, 8] and in a bubble chamber.[10] In this experiment we have observed some 500 annihilations. Detailed measurements were possible on 437 annihilations, of which 140 fit requirements of annihilation on hydrogen. The remaining 297 annihilations, all of which can definitely be attributed to carbon, fall into two approximately equal groups: those which appear to occur after the antiproton has come to rest (or has at most 50 Mev kinetic energy), and those in which the antiproton still has significant kinetic energy (at least 50 Mev) upon fatal collision with a carbon nucleus. Both the hydrogen and the carbon annihilations will be discussed in detail in the following sections.

The characteristic nucleon-antinucleon annihilation proceeds through the creation of pions, both charged and neutral. In about 4% of the annihilations at low antiproton kinetic energy, a pair of K mesons is created. No other direct product has yet been observed.

In the next few pages we will discuss the methods we have used to observe the various kinds of annihilation products.

Protons and Charged Pions. The pion products from a fundamental $N\bar{N}$ annihilation within a carbon nucleus may interact before getting our of the nucleus. Such an interaction may give rise to protons, neutrons, and other nuclear fragments. The charged prongs from these stars are directly observable in the chamber and in many cases may be identified on the basis of momentum, charge, and density of track. Distinction between pions and protons is usually straightforward, except in rare cases of high-momentum positive tracks. When dealing with the black prongs, however, we are unable to distinguish between short-range protons and deuterons or other charged nuclear fragments. For convenience, all these heavy prongs are assumed to be protons.

A charged prong is considered identified once it has been designated as a π^+, a π^-, or a heavy prong (p^+). As we pointed out in Section II D, such a designation is made only after the scanner's tentative identification, based on bubble-count ionization measurements, is confirmed by the measured momentum.

Charged-particle identification breaks down for steep tracks. Here the momentum of the particle may be parallel to the magnetic field, so that not even the sign of the charge can be determined. Furthermore, even a minimum track looks dense in a projected view because the cameras are above the chamber. We have used two approaches to this problem:

(a) A compilation of all completely identified stars was made. Then each annihilation with one or more prongs undetermined was compared with the list of known stars. An assignment of particle identity (pion or proton) or particle charge (for pions only) was made in ratio to the frequency among the known stars of the various possible final configurations of the unknown star. To gain an idea of the numbers involved, consider the carbon annihilation at rest. In these, 65% of the annihilations had complete prong identification,[38] 75% had no unidentified particle, and 80% had no unidentified charge. Furthermore, 90% of the prongs in this group of annihilations were identified.

(b) A compilation was made of all annihilation products, listing total number identified for each kind of particle. A separate listing was made for prongs of dubious identity or charge. These latter, amounting to 10% of all the prongs, were then assigned in blocks according to the over-all frequency of identified particles, without regard for specific stars. The result obtained was an average multiplicity of π^+, π^-, and p^+ for the group of stars under consideration. This process was repeated, using only those annihilation products having dip angles within 30° of the horizontal. This region constitutes half of the solid angle.[39] Elimination of steep dip angles enables more confident identification of particles, and only 5% of all prongs in this sample were undetermined. Multiplicities determined in this way were in good agreement

with those obtained for the whole solid angle and with those obtained by the method of detailed correction described in (a) above.

Detection efficiency for charged pions was about 99%. This estimate is based in part on a scanning-efficiency calculation based on the results of the two independent scans, and in part on the consideration of the two effects that can render pions unobservable. One of these effects is pion charge exchange or absorption near the annihilation origin, while the other is antiproton annihilation so close to the chamber top or bottom that particles can go out unobserved. Both effects together account for about 0.5% of the charged pions. The other common pion interactions, namely elastic scattering and pion decay, still allow the pion to be detected. Even for pion decay at rest near the annihilation, the characteristic $\pi \rightarrow \mu \rightarrow e$ decay scheme is easily identified through the 3-mm range of the μ and the usually visible (at least 98% of the time) electron.

Neutral Pions and Other Neutral Products. Uncharged annihilation products may occasionally be observed. The decay of neutral K mesons within a few centimeters of the annihilation makes detection extremely probable for the mode of decay in which 2 charged particles appear. This is discussed more fully in a later section.

Neutrons ejected from carbon stars, however, are essentially undetectable because their reactions with charged particles, such as n-p elastic scattering, do not allow unique association with the annihilation. No attempt was made to observe neutrons from annihilations.

Neutral pions may be observed infrequently through the pair-conversion of a photon decay products. The number of neutral pions is related to the number of observed electron-positron pairs through two factors, the mean free path for pair production in the propane and the chamber geometry. The mean free path for pair production is a function of the energy of the photon, varying from 200 g/cm^2 (480 cm) of propane at 20 Mev to 64 g/cm^2 (154 cm) at 1000 Mev.[40] The problem of chamber geometry was solved by establishing an arbitrary fiducial volume within

the chamber. This volume was a rectangular parallelopiped slightly smaller than the chamber and contained all of the annihilations. Only photons that converted within this volume were accepted. Each observed pair was weighted by a factor $(1 - e^{-\frac{\ell_v}{\ell_p}})^{-1}$, where ℓ_p is the mean free path for photon conversion into a pair of the observed energy, and ℓ_v is the distance from the annihilation to the fiducial-volume boundary along the photon line of flight. The observed electron pairs were corrected for energy loss before calculation of the weighting factor.

From the results of the two independent scans, we concluded that the scanning efficiency for pairs within the fiducial volume was 98.5%. About 7% of all the π^0-decay photons converted into pairs within the volume. This means that our π^0 detection efficiency was 14%.

A check for possible "accidental" pairs was made by scanning a section of film for pairs that appeared to originate from an arbitrary point near the center of the bubble chamber. This check indicated that approximately 2% of the observed annihilation-associated pairs should be accidental. Both this factor and the scanning efficiency factor, which tend to balance each other, are considered negligible.

Dalitz Pairs. A consideration of annihilation products would not be complete without some reference to Dalitz pairs. In one of every 80 π^0 decays, a photon materializes directly as an electron-positron pair. These electron pairs look like direct annihilation products, because the π^0 lifetime, $\tau \lesssim 4 \times 10^{-16}$ sec,[41] does not allow physical separation of the pair origin from the annihilation origin in the bubble chamber. If the electron path length is long enough--e. g., at least 10 cm--then an experienced scanner may recognize it by its high rate of energy loss (radiation loss by an energetic electron). A low-energy electron is easily recognized by its characteristic spiral stopping.

Among the products of almost 500 annihilations, we have tentatively identified 6 Dalitz pairs. If we assume that each annihilation produces 1.6 neutral pions and, of these, 0.2 are absorbed in each carbon star, then we should expect to see 9 Dalitz pairs. This is considered satisfactory agreement with observation.

K Mesons. The strange-particle K-meson products of annihilation are discussed in Section V D.

B. The Hydrogen Annihilation

In this section we present the results of measurements made on 140 stars that meet the conditions for antiproton annihilation in hydrogen. It is estimated that about 40 of these events are actually annihilations on carbon nuclei. Because it is impossible to determine which hydrogen-like annihilations are genuine and which are not, all are included in a single group which is considered to be typical of the $\bar{p}$-H annihilation.[42] For these annihilations, the average kinetic energy of the antiproton was 80 Mev.

The multiplicity of charged mesons per hydrogen annihilation was found to be 3.06 ± 0.12.[43] The average energy (including rest energy) was 390 ± 14 Mev per charged meson. We have also observed 29 gamma-ray pair-conversions which give 1.6 ± 0.5 neutral pions per annihilation. The π^0 total energy averaged 356 ± 110 Mev. Combining, we have an observed multiplicity of 4.7 ± 0.5 pions per annihilation. In addition, some 4% of these annihilations produced K mesons (based on six events, one of which is classified as uncertain).

The error in our observed pion multiplicity of 4.7 ± 0.5 pions per annihilation is mostly due to the large error in the neutral-pion multiplicity. If we consider only charged pions, we may still calculate a combined charged- and neutral-pion multiplicity if we make two assumptions: (a) the neutral pions have the same average total energy (390 ± 14 Mev) as the charged pions, and (b) all of the annihilation energy that does not appear in K mesons is carried off by pions. Using these assumptions, we get a pion multiplicity of 4.88 ± 0.18 pions per annihilation. By subtracting the observed charged-pion multiplicity of

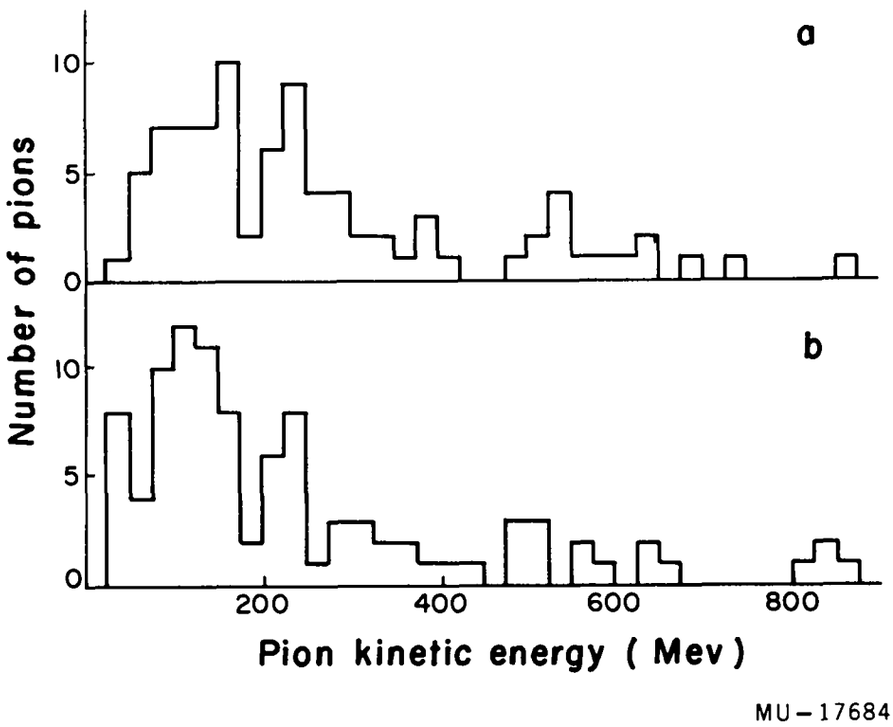

Fig. 14. Kinetic-energy spectra of the charged pions from hydrogen annihilations. Only pions with at least 10 cm of track (unless stopping) and which make an angle of $\gtrsim 60^{\circ}$ with the magnetic field are included.
(a) π^- spectrum, (b) π^+ spectrum.

3.06 ± 0.12 from 4.88 ± 0.18, we get a difference of 1.82 ± 0.21 pions per star that can be attributed to neutral pions. These results are consistent with the production of equal numbers of π^+, π^-, and π^0 mesons, although such a division is not specifically required for $\bar{p}p$ annihilations.

The kinetic-energy spectrum of the observed charged pions is presented in Fig. 14. Only those pions that make an angle of at least 60° with the magnetic field and that have at least 10 cm of measurable track (unless stopping) are included. Only 99 of the π^+ mesons meet these conditions (Fig. 14a). The average π^+ kinetic energy is 240 ± 19 Mev. Eighty-six of the π^- mesons are plotted in Fig. 14b. The average π^- kinetic energy is 263 ± 21 Mev. The most probable kinetic energy for both π^+ and π^- is approximately equal to the pion rest mass, giving a most probable total energy of about twice the pion rest mass.

Figure 15 shows an energy distribution of photon pair-conversions. These photons are decay products of π^0 mesons created in the hydrogen-like annihilations. Each photon plotted in Fig. 15 has been weighted according to its probability of converting within the chamber. For a π^0 kinetic-energy spectrum similar to the π^+ or π^-, the most probable γ energy is half the π^0 rest mass, or 68 Mev. Our most probable value seems to be more than 100 Mev, but we must acknowledge the poor statistics. When all photons, including those from carbon annihilations(see next section), are considered, the resulting energy spectrum shows good agreement with the predicted value of 68 Mev.

The over-all results for hydrogen-like annihilations are presented in Table VI. A more detailed breakdown is presented in Table VII. The data show that the hydrogen annihilation produces 4 charged mesons in about 50% of the events, while 40% have only two charged mesons. The remaining 10% is almost equally split between 0-prong and 6-prong stars. The π^0 multiplicity decreases as the $\pi^\pm$ multiplicity increases. With poor statistics, we find $2.4^{+1.2}_{-0.9}$ neutral pions per 2-prong star, and $1.1^{+0.9}_{-0.5}$ per 4-prong star.

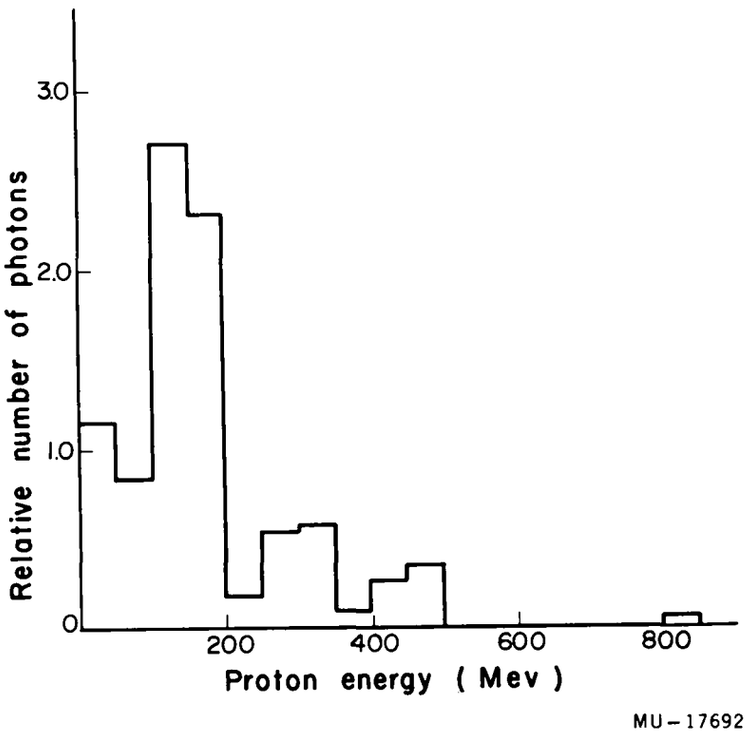

Fig. 15. Energy histogram of 29 π^0-decay γ conversions observed in hydrogen annihilations. Each photon has been weighted according to its conversion probability. Because of the effect of the weighting factor, each unit of the ordinate represents 50 photons.

Table VI

Summary of hydrogen-like annihilations, based on 139 events.

Annihilation product	Average multiplicity	Energy per particle[a] (Mev)	Energy per annihilation (Mev)
Charged pions	3.06 ± 0.12	390 ± 14	1195 ± 62
Neutral pions[b]	1.6 ± 0.5	356 ± 110	570 ± 250
K mesons	0.08 ± 0.02	606 ± 77	49 ± 15
			1814 ± 258 (total)

[a]Includes rest mass.

[b]Neutral-pion results appearing in this table were obtained by observation (through pair production) of about 7% of the decay photons. The π^0 multiplicity becomes 1.82 ± 0.21 if we assume that the average π^0 energy is the same as for charged pions.

Table VII

Breakdown of hydrogen-like annihilations.

Five events in which K mesons were produced are excluded.

Charged-pion multiplicity	Number of events	Energy per charged pion[a] (Mev)	Number of photon pairs	Neutral pion multiplicity	Energy per neutral pion[a] (Mev)
0	8	---	3	(~3.5)[b]	*
2	54	424	15	$2.4^{+1.2}_{-0.9}$	365
4	67	378	10	$1.1^{+0.9}_{-0.5}$	330
6	6	310	1	(~1)[b]	*

[a]Includes rest mass.

[b]Small number of observed photons allows only a rough estimate.

*Statistics too poor to give a number.

Our results should be compared with the hydrogen bubble-chamber results of Horwitz, Miller, Murray, and Tripp,[10] who have studied 81 antiproton annihilations at rest. They have found 3.21 ± 0.12 charged mesons per annihilation. Their average for the $\pi^{\pm}$ energy (including rest mass) was 380 ± 12 Mev per pion. In other respects there is also good agreement. For example, they have also reported that 50% of the hydrogen annihilations have 4 prongs, while about 40% have 2 prongs.

It is also of interest to compare our results with the predictions of the several theories. The Fermi statistical model has been discussed extensively elsewhere in connection with antinucleon-nucleon annihilation.[7, 8, 10, 11] The straightforward application of the Fermi theory predicts a low pion multiplicity (3.3 pions per annihilation when K production is ignored, and even fewer when K production is considered) and a high K probability (as much as 41%). The Fermi model can be brought into agreement with experimental results of almost 5 pions per annihilation by increasing the interaction volume $\Omega = 4/3\ \pi\ (\hbar/m_{\pi}c)^3$ by a factor of ten, but even then the theory predicts about three times as many K mesons as were observed. Attempts to improve this theory by minor changes have so far been unsuccessful. As discussed by Sudershan,[44] enhancement of pion multiplicity can be obtained by considering a strong pion-pion interaction.

The theory of Koba and Takeda suggests that annihilation pions have two distinct origins: first, the meson cloud which gives 2.6 pions; and second, the nucleon core which adds 2.2 pions. This model is based on the idea that pion-cloud oscillation times are long compared to the core-annihilation time. Upon overlap of nucleon-antinucleon cores, annihilation proceeds, leaving some of the pions in the cloud. The reduced energy available to core annihilation is treated with the Fermi theory. The model predicts 4.8 pions per annihilation, which is in good agreement with the experimental results. However,

recent calculations by Frautschi[45] indicate that the K-multiplicity predictions of the Koba-Takeda model are too high by a factor of about 4.

C. The Carbon Annihilation

Description of the Carbon Star

We have divided all the antiproton annihilations in carbon into two groups: those which annihilate in flight, and those which annihilate at rest. An antiproton kinetic energy of 50 Mev was picked as a dividing line, and all antiproton annihilations at less than 50 Mev were considered at rest. In the energy region from 50 Mev to 200 Mev, 151 antiprotons of 120-Mev average kinetic energy annihilated with products that clearly identified the event as occuring on a carbon nucleus. As pointed out earlier, a correction must be made for carbon annihilations that are indistinguishable from hydrogen stars. Using the method described in Section IIID, we estimate that 15 "fake" $\bar{p}$-H annihilations should be added to the identified carbon stars, to give a total of 166 in-flight carbon annihilations. Similarly, we have identified 146 carbon annihilations at rest and apply a correction of 25 fake $\bar{p}$-H stars to obtain a total of 171 at-rest carbon annihilations.

We have carried out a parallel analysis on the two groups of carbon annihilations. All the tables listing results compiled from the carbon stars have separate columns for in-flight and at-rest events. All graphs and plots are duplicated in a like manner, so that a glance at a single figure allows quick comparison between similar quantities derived from at-rest and in-flight annihilations.

The products from carbon stars are primarily pions and heavy prongs. For convenience, all the heavy prongs have been classified as protons, with a lower cutoff of 10 Mev, which corresponds to a proton range of 2mm. The annihilation multiplicities for the in-flight stars are $1.65 \pm 0.09\ \pi^-$ per star, $1.31 \pm 0.10\ \pi^+$ per star, $1.16 \pm 0.40\ \pi^0$ per star, and $1.58 \pm 0.10\ p^+$ per star. For the at-rest annihilations, we get $1.50 \pm 0.10\ \pi^-$ per star, $1.35 \pm 0.12\ \pi^+$ per star, $1.14 \pm 0.40\ \pi^0$ per star, and $1.03 \pm 0.08\ p^+$ per star. These results are also shown in Table VIII. The combined total pion multiplicity, charged plus neutral, is seen to be about 4.1 ± 0.3 pions per star. This is significantly less than the 4.7 ± 0.5 pions observed in hydrogen annihilations, and this difference as well as other features of the carbon annihilation is discussed in the following section.

The kinetic-energy spectra for positive and separately for negative pions produced in these carbon annihilations are given in Fig. 16. As in the case of the hydrogen annihilation, only those pions which had 10 cm of measured path (unless stopping) and which made an angle of at least 60° with the magnetic field were included in the energy spectra. These same conditions were applied to get the proton energy spectra shown in Fig. 17. The average kinetic energies from the in-flight annihilations were as follows: 86 π^+ gave $\overline{T} = 242 \pm 19$ Mev, 106 π^- gave $\overline{T} = 215 \pm 17$ Mev, and 136 p^+ above a 10-Mev cutoff gave $\overline{T} = 68$ Mev. Average kinetic energies from the at-rest annihilations were as follows: 86 π^+ gave $\overline{T} = 223 \pm 18$ Mev, 101 π^- gave $\overline{T} = 239 \pm 19$ Mev, and 76 p^+ above a 10-Mev cutoff gave $\overline{T} = 75$ Mev.

The photon energy spectra arising from π^0 decays are given in Fig. 18. Twenty-three photon-produced pairs were measured to produce the plot associated with in-flight annihilations, while 25 pairs were associated with the at-rest annihilations. The weighted average energy for both types of annihilation was 171 Mev per pair, giving an average π^0 total energy of 342 ± 120 Mev.

A detailed breakdown of the carbon annihilations is given in Table IX. Here the annihilations are classified according to the number of heavy prongs. For example, all annihilations which produced only one black prong, regardless of its energy, are treated as a separate group.

Table VIII

Multiplicities and energies of the principal products of carbon annihilations

	In-flight stars 166 events		At-rest stars 171 events		Combined 337 events	
Product	Multiplicity	Energy[a]	Multiplicity	Energy[a]	Multiplicity	Energy[a]
π^-	1.65±0.09	354±17	1.50±0.10	378±19	1.58±0.07	366±13
π^+	1.31±0.10	381±19	1.35±0.12	362±18	1.33±0.08	371±13
π^0	1.16±0.40	342±120	1.14±0.140	343±120	1.15±0.30	342±90
$p^{+(b)}$	1.58±0.10	68	1.03±0.08	75	1.29±0.07	71

[a]Total energy is given for pions, kinetic energy for protons.

[b]This includes all heavy charged particles with propane range greater than 2 mm, which is the range of a 10-Mev proton. See Fig. 17 for the p^+ energy spectrum.

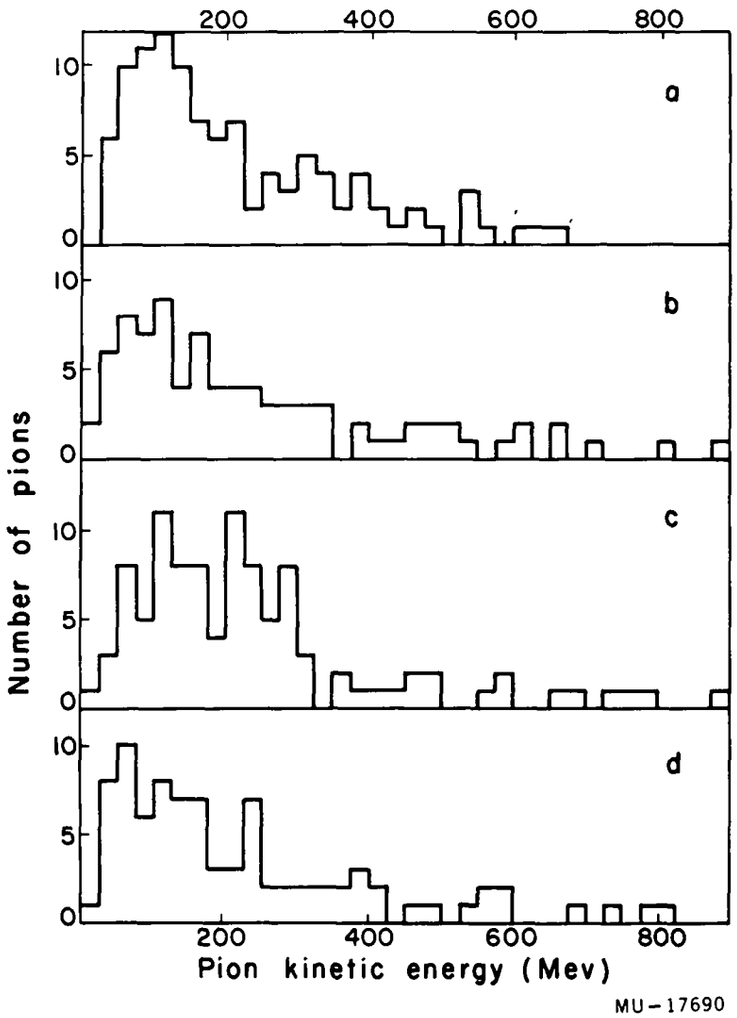

Fig. 16. Kinetic-energy spectra of charged pions from carbon annihilations. Only pions with at least 10 cm of track (unless stopping) and which make an angle of $\gtrsim 60^{\circ}$ with the magnetic field are included. (a) π^- spectrum for in-flight carbon stars, (b) π^+ spectrum for in-flight carbon stars, (c) π^- spectrum for at-rest carbon stars, and (d) π^+ spectrum for at-rest carbon stars.

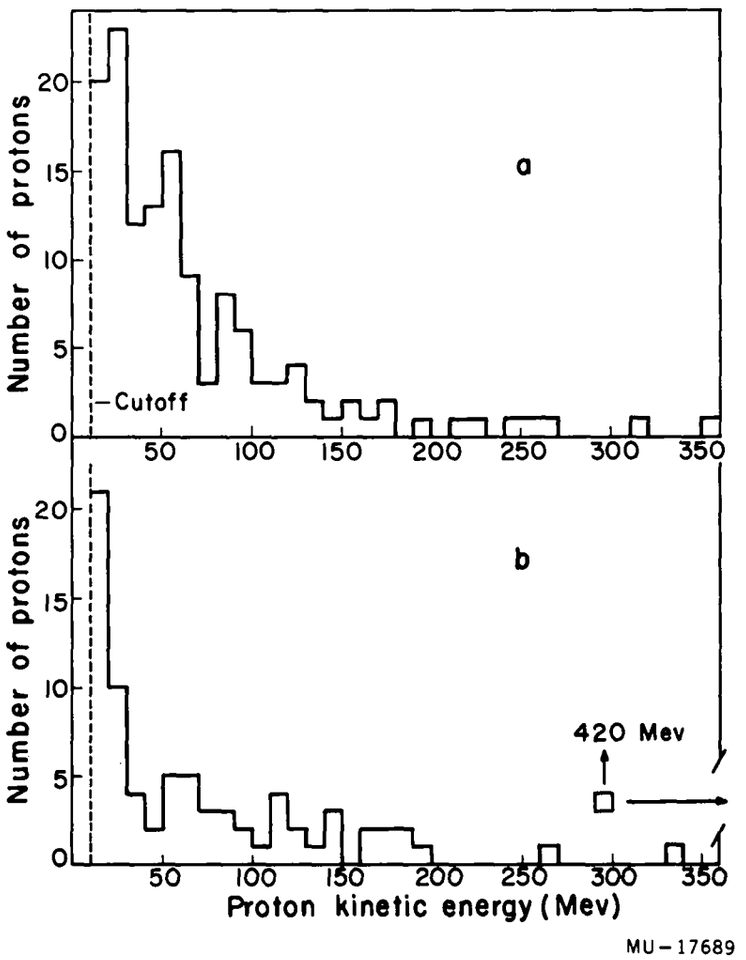

Fig. 17. Kinetic-energy spectra of black prongs (all assumed to be protons) from carbon annihilations (a) in flight (Fig. 17a) and (b) at rest (Fig. 17b). Only particles with at least 10 cm of track (unless stopping) and which make an angle of $\gtrsim 60^{\circ}$ with the magnetic field are included.

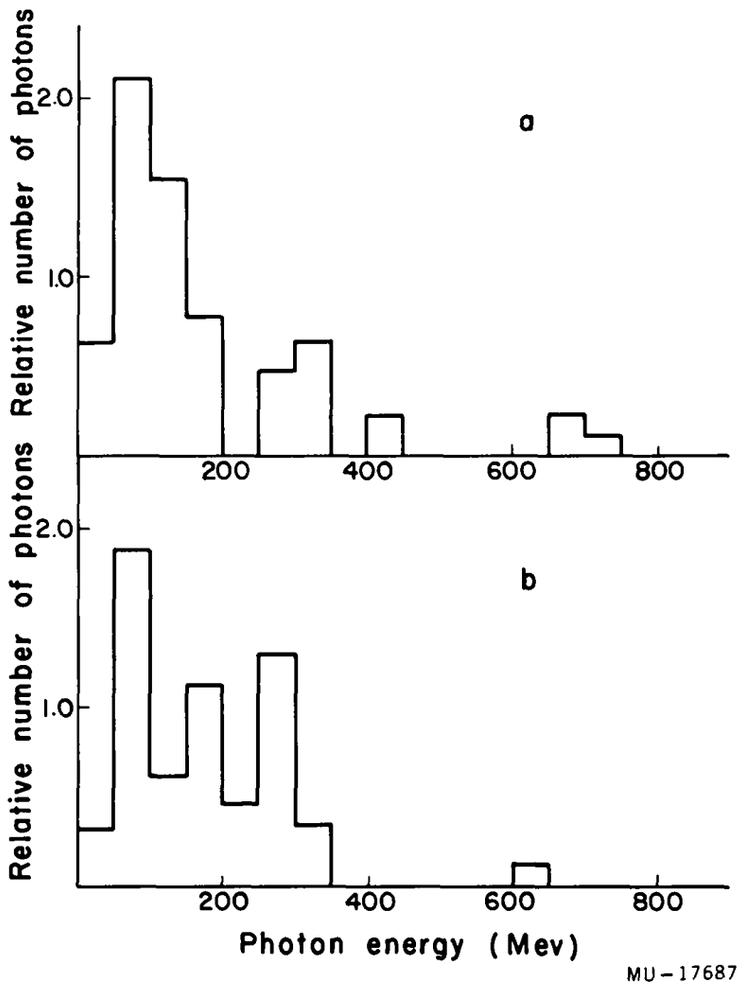

Fig. 18. Energy histograms of 23 π^0-decay γ conversions observed in (a) in-flight carbon annihilations and (b) 25 γ conversions observed in at-rest carbon annihilations. Each photon has been weighted according to its conversion probability. Because of the effect of the weighting factor, each unit on the ordinate represents 50 photons.

Table IX

Multiplicities and energies of the principal products of several types of carbon annihilation.

Type of annihilation	Product	In-flight stars		At-rest stars		Combined	
		Multiplicity	Energy (Mev)	Multiplicity	Energy (Mev)	Multiplicity	Energy (Mev)
$\bar{p}$-C stars with no heavy prongs	π^-	1.74	370	1.67	369	1.70	369
	π^+	1.47	379	1.43	363	1.45	370
	π^0	1.60	484	1.60	378	1.60	431
	p^+	0	--	0	--	0	--
		38 events		72 events		110 events	
$\bar{p}$-C stars with one heavy prong	π^-	1.73	344	1.57	387	1.65	364
	π^+	1.50	381	1.28	339	1.40	361
	π^0	0.83	322	0.70	272	0.77	300
	p^+	1.0	--	1.0	--	1.0	--
		52 events		46 events		98 events	
$\bar{p}$-C stars with two heavy prongs	π^-	1.47	341	1.26	384	1.38	358
	π^+	1.30	349	1.33	417	1.31	378
	π^0	1.00	336	1.23	312	1.10	326
	p^+	2.0	--	2.0	--	2.0	--
		36 events		27 events		63 events	
$\bar{p}$-C stars with more than two heavy prongs	π^-	1.61	333	1.48	341	1.56	336
	π^+	1.00	427	1.32	316	1.12	377
	π^0	1.30	258	0.60	284	1.03	264
	p^+	3.7	--	3.4	--	3.6	--
		41 events		25 events		66 events	
$\bar{p}$-C stars with one energetic proton ($T_{p^+} > 40$ Mev)	$\pi^\pm$	3.18	--	2.24	--	2.71	--
	π^0	1.60	--	1.24	--	1.42	--
	p^+	1.00	83	1.00	98	1.00	90
		17 events		17 events		34 events	

Groups were set up for annihilations with 0, 1, 2 and ≥ 2 black prongs. A final group--really a subgroup of the group with 1 black prong--included only stars with purely pionic products except for one energetic proton ($T > 40$ Mev). Pion multiplicities and energies are given for each group. In some cases, the number of events is too small to give statistically sound results, particularly for neutral pions.

The distribution of annihilations according to the total number of charged prongs from the stars is shown in Fig. 19. A more informative prong-frequency distribution in which only the pions are considered is given in Fig. 20. This pion frequency distribution is also given in Table X, where the π^0 multiplicity is included, showing the decrease in π^0 mesons along with an increase in the number of charged pions. This was also noticed in the hydrogen annihilation.

The distribution of carbon annihilations according to the net charge of their pion products is presented in Table XI. All heavy prongs were ignored in preparing this table. It is seen that most annihilations have a net pionic charge of either $\Sigma q = 0$ or $\Sigma q = -1$. This is to be expected for simple $\bar{p}p$ or $\bar{p}n$ annihilations. However, 25% of the carbon annihilations have $\Sigma q \neq 0$ or -1. Another interesting fact is that the surplus of negative charge is only 0.25 π^- per annihilation. An interpretation of this data, leading to conclusions about the $\bar{p}p$ and $\bar{p}n$ annihilation ratio within the carbon nucleus will be attempted in the next section.

A carbon annihilation of especial interest is the neutron-type annihilation. We have observed 40 annihilations on carbon nuclei which simulate free $\bar{p}n$ annihilations. These events, all of which were purely pionic and had an excess of one negative pion, were divided as follows:

Number of charged pions	1	3	5	7
Number of events	9	18	12	1

The charged-pion multiplicity was 3.25 ± 0.25 $\pi^{\pm}$ per annihilation. The average energy per pion was 362 ± 24 Mev, including the $\pi^{\pm}$ rest mass. Eleven gamma-ray-pair conversions (5 on 3-prong stars and 6 on 1-prong stars) gave $1.8^{+1.1}_{-0.7}$ π^0 per annihilation. The π^0 total energy averaged 444 ± 197 Mev. Combining the charged and neutral pions, we get $5.05^{+1.1}_{-0.7}$ pions for a total of 1976 Mev per annihilation (one event giving K mesons was excluded).

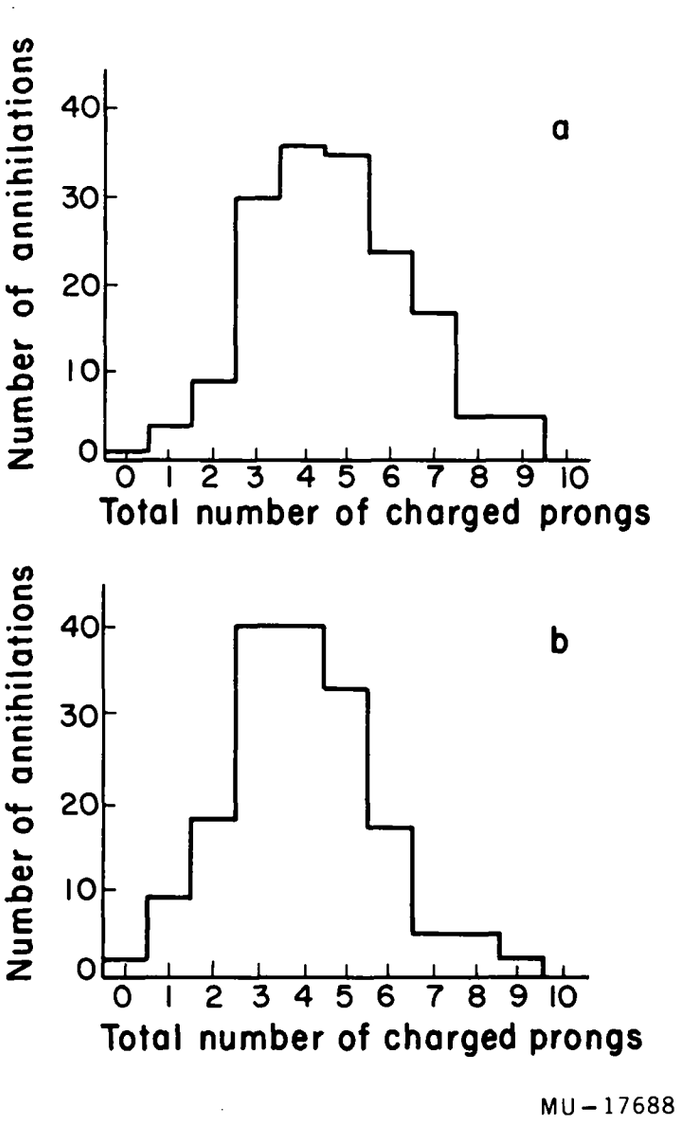

Fig. 19. Frequency distribution of carbon annihilations according to the total number of charged prongs observed for (a) in-flight carbon stars and (b) at-rest carbon stars.

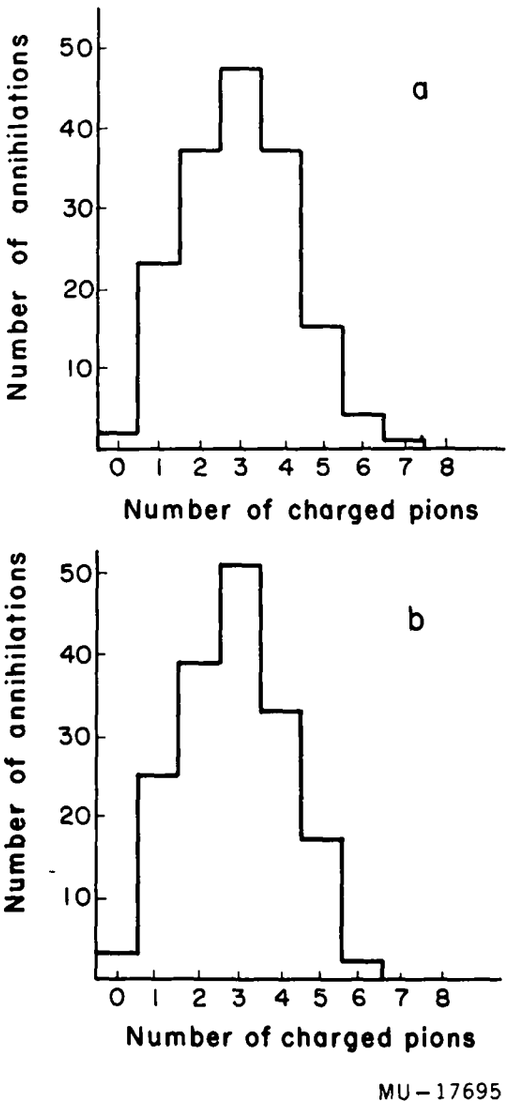

Fig. 20. Frequency distribution of carbon annihilations according to the total number of charged pions observed for (a) in-flight carbon stars and (b) at-rest carbon stars. Black prongs were ignored in constructing this histogram.

Table X

Pion frequency distributions observed in $\bar{p}$-C annihilations.[a]

Number of charged pions	In-flight stars		At-rest stars		Combined	
	Number of stars	π^0 multiplicity	Number of stars	π^0 multiplicity	Number of stars	π^0 multiplicity
0	2	(~2)	3	(~2)	5	(~2)
1	23	2.0	25	2.6	48	2.3
2	37	1.4	39	1.2	76	1.3
3	47	1.8	51	1.2	98	1.5
4	37	0.2	33	0.5	70	0.4
5	15	-	17	-	32	-
6	4	-	2	-	6	-
7	1	-	0	-	1	-

[a]All heavy-prong annihilation products were ignored in compiling this data.

Table XI

Distribution of carbon annihilations according to net charge of their pion products

Net charge	In-flight stars	At-rest stars	Combined	Predicted
-3	1	0	1	2
-2	10	5	15	22
-1	62	64	126	132
0	64	67	131	130
+1	24	26	50	46
+2	5	9	14	5
+3	0	0	0	0

The above results may be regarded as giving an indication of the details of the $\bar{p}n$ annihilation.

A breakdown of the energy observed from carbon stars is presented in Table XII.

Table XII

Breakdown of the energy observed from carbon stars.

	In-flight stars	At-rest stars
Energy expected (Mev)	1996	1876
Energy observed (Mev):		
π^-	584 ± 42	566 ± 47
π^+	500 ± 45	488 ± 50
π^0	397 ± 197	391 ± 188
Nucleons	> 212	> 164
K	49 ± 15	49 ± 15
Total observed	> 1742 ± 207	> 1658 ± 200

Interpretation of the Carbon Star

Pion absorption. The first notable characteristic of the carbon annihilation is the decreased pion multiplicity from that observed in hydrogen. This decrease is not regarded as likely to be due to a significant difference in the primary nucleon-antinucleon annihilation, but is attributed to absorption of pions by the residual nucleus. This interpretation is borne out by the presence of the heavy prongs.

Heavy prongs from a carbon annihilation might have five different origins:

(1) The absorption of an annihilation pion in the residual nucleus. This is pictured as a three-body interaction--the inverse of the pion production reaction $N + N \rightarrow \pi + N + N$.

(2) The inelastic[46] or charge-exchange scattering of one of the annihilation pions on one of the residual nucleons.

(3) The quasi-elastic scattering of a proton by an antiproton which subsequently annihilates in the same nucleus.

(4) The evaporation of nucleons from an excited residual nucleus.

(5) The possibility that the annihilation involves directly two or more nucleons, wherein nucleons or nuclear fragments may obtain annihilation energy without an intermediate state of real pions.

Only the first two processes are regarded as important to the explanation of observed multiplicities and energies of the pions. Evaporation prongs (Process 4) can appear in association with any of the other interactions, and no serious effort will be made to investigate them. Processes 3 and 5 will be ignored.[47]

Processes 1 and 2 can be pursued further on the basis of a very simplified approach. We assume that a pion interacts only once before leaving the nucleus. This assumption is justified on the grounds that the mean free path for scattering in nuclear matter is greater than the nuclear radius except at the πN resonance. Moreover, the assumption is supported by the report that for π^- incident on carbon nuclei (in great contrast to heavier nuclei), the angular distribution for inelastic scattering is similar to that expected for scattering on free nucleons.[48]

We have taken the mean free paths for pion scattering and absorption in nuclear matter as a function of energy[49] and weighted them according to our observed energy spectrum of pions from hydrogen annihilations. This gives us the relative number of pions that are scattered and absorbed as a function of pion energy. We estimate from these calculations that absorption occurs half as often as scattering, and that the average kinetic energy of the absorbed pion is $\bar{T}$ = 315 Mev, while for scattering the average is $\bar{T}$ = 240 Mev.

An absorption of a pion at $\bar{T}$ = 315 Mev should release $T + M_\pi$ = 454 Mev to the nucleons involved. Furthermore, since the absorption occurs preferentially at high pion energies, the observed pion energy spectrum will be altered by their disappearance.

Further calculations show that the average change in kinetic energy of a pion in a scattering process is $\Delta\bar{T}$ = -60 Mev. This has been weighted over the pion energy spectrum and averaged over the scattering angular distribution.

Combining the absorption and scattering in the ratio of two scatters per absorption, we expect that 80% of the energy given to nucleons is due to pion absorption. This energy can not all be observed directly because neutrons, which are assumed to carry off half the energy, are invisible. We must also correct for the unobserved black prongs below our 2-mm cutoff. We estimate this correction by a very short extrapolation of the distribution of protons vs energy (see Fig. 17). From this extrapolation, we estimate that the correct p^+ multiplicity is 2.0 p^+ per in-flight carbon star, and 1.55 p^+ per at-rest carbon star, still assuming that all black prongs are protons. The corrected average kinetic energy is $\bar{T}$ = 53 Mev per proton, both in flight and at rest. The presence of deuterons, alpha particles, etc., among the black prongs tends to increase the average energy per prong. We have the following situation for carbon stars:

	in flight	at rest
estimated multiplicity of black prongs	2.0	1.55
estimated energy in black prongs per star	> 106 Mev	> 82 Mev
estimated energy in nucleons per star	> 212 Mev	> 164 Mev

We may now compute the pion multiplicities for carbon stars, after correcting for absorption and scattering. These are:

	in flight ($\bar{T}_{p^-}$ = 120 Mev)	at rest
pion multiplicity (observed)	4.1 ± 0.4	4.0 ± 0.4
energy in nucleons per star	> 212 Mev	> 164 Mev
pion multiplicity (corrected)	> 4.5 ± 0.5	> 4.3 ± 0.5

These numbers should be compared with a pion multiplicity of 4.7 ± 0.5 at $\bar{T}_{p^-}$ = 80 Mev for our hydrogen annihilations.

Now consider the pion energy spectra in carbon and hydrogen. Because the errors on π^0 energies are large, we consider only the charged pions for comparison. All carbon annihilations give average total energy $\bar{E}$ = 368 ± 9 Mev per charged pion, while the hydrogen annihilations give $\bar{E}$ = 390 ± 14 Mev. With our crude model wherein absorption occurs half as often as scattering, a 22-Mev change in average pion energy is expected when 0.5 pions are absorbed per carbon annihilation.

We conclude that the pion absorption in carbon amounts to ~ 0.6 pions per annihilation, which is the result of subtracting the directly observed carbon multiplicity of 4.1 from the hydrogen multiplicity of 4.7. This absorption of ~ 0.6 pions per annihilation is confirmed by the energy observed in black prongs (which is consistent with > 0.4 pions absorbed) and with the observed average pion energy (which is consistent with 0.5 pions absorbed). We further conclude that our assumption that the primary $N\bar{N}$ annihilation within the carbon nucleus has the same products as a free $N\bar{N}$ annihilation is essentially correct.

In-flight vs at-rest stars. The mean free path for antiprotons in nuclear matter is about 0.6×10^{-13} cm at 100 Mev.[50] This means that nearly all annihilations occur on the nuclear surface. Previous reports, based on emulsion studies, have suggested that significant differences between in-flight and at-rest black-prong multiplicities stem from the surface annihilation of at-rest antiprotons as contrasted with the deeper nuclear penetration of more energetic antiprotons.[7,8] Our data lead

us to believe that deeper penetration is not the prime factor necessary to explain carbon results. An alternative explanation of in-flight and at-rest differences is based on a feature of the annihilation in flight that has escaped comment heretofore.

We have observed that, for in-flight carbon stars, black prongs are more frequent and that more energy appears in nucleons, suggesting a difference in pion absorption. But we have also observed an expected forward-backward asymmetry in pions produced by in-flight annihilations. This asymmetry indicates that 1.4 pions are produced in the forward hemisphere for each one produced backward at $\bar{T}_{\bar{p}} = 120$ Mev in carbon. We assume that annihilation occurs at a depth such that the effective solid angle subtended by the nucleus approaches 2π (i.e. near the nuclear surface). We further assume that the 120-Mev average kinetic energy (lab) of the incident antiproton should cause an increase of ~ 0.15 pions in the observed multiplicity.[51] These two assumptions lead to a predicted difference in pion absorption that almost accounts for the energy observed in nucleon products for in-flight and at-rest carbon stars. Probably the only conclusion which can be derived from this result is that really significant differences in carbon nucleus penetration do not occur for in-flight and at-rest annihilations. This implies that the mean-free-path for antiproton annihilation in nuclear matter remains short (less than a fermi) for energies up to 200 Mev.

Pion net-charge distribution. It was pointed out in the previous section that most annihilations in carbon have a net pion charge of either $\Sigma q = 0$ or $\Sigma q = -1$. This is expected on the basis of simple $\bar{p}p$ and $\bar{p}n$ annihilations within the carbon nucleus, followed by pion charge exchange and absorption reactions that obey charge independence.

Actually, even with equal $\bar{p}p$ and $\bar{p}n$ annihilation cross sections, we do not expect the difference in average multiplicity to be $n(\pi^-) - n(\pi^+) = 0.5$ (which would obtain for free protons and neutrons), for the reasons given below. Pion absorption alone, assumed equally probable for charged and neutral pions, reduces the π^- excess to $0.43\ \pi^-$ per carbon annihilation. Furthermore, an original excess of π^- means that more π^- undergo charge exchange. Still another process

that reduces the expected π^- excess in carbon annihilations is the two-step interaction $\bar{p} + p \rightarrow \bar{n} + n$ (in carbon) followed by $\bar{n}$ annihilation within the same carbon nucleus (this can even give a net pion charge $\Sigma q = +1$). After considering all of these effects, we are able to calculate an expected pion net-charge distribution for the carbon annihilations. The calculation is based on the following assumptions: (a) $\bar{p}p$ and $\bar{p}n$ annihilations are equally probable within the nucleus, (b) the probabilities for the various annihilation modes for $\bar{p}p$ and $\bar{p}n$ are the same as given in Table VII and on page 60 , (c) 0.6 pions are absorbed per star (absorption is assumed equally probable for π^+, π^-, and π^0), (d) 1.2 pions are scattered per star (all are assumed to occur in the I = 3/2 state) and (e) $\bar{p}p$ charge exchange with subsequent annihilation occurs 0.15 times as often as $\bar{p}p$ annihilation. The results of the calculation are given in Table XI. The predicted distribution gives a difference in average multiplicity of $n(\pi^-) - n(\pi^+) = 0.38$, and it fits the observed distribution with minor deviations.

We can summarize our results as follows:

Pion excess per annihilation	In flight	At rest	Combined	Predicted
$n(\pi^-) - n(\pi^+)$	0.34±0.13	0.15±0.15	0.25±0.11	0.38

These results do not allow any emphatic conclusions. In particular, the discrepancies are not considered sufficient to alter our assumption of equally probable $\bar{p}p$ and $\bar{p}n$ annihilations within carbon at this time, although the possibility of a difference is suggested by our at-rest data. Such a possibility has been suggested by Amaldi,[52] but must be verified by further experiment.

D. Strange Particles

The nucleon-antinucleon annihilation process is able to produce a pair of K mesons. This is predicted[53] as well as observed.[7] Our large propane chamber is highly efficient for the observation of short-lived neutral K mesons, an example of which is seen in Fig. 21. Charged K mesons can also be detected in the case of long tracks under good ionization conditions, and of course, when they decay within the chamber. An example of K^+ decay at rest is shown in Fig. 22.

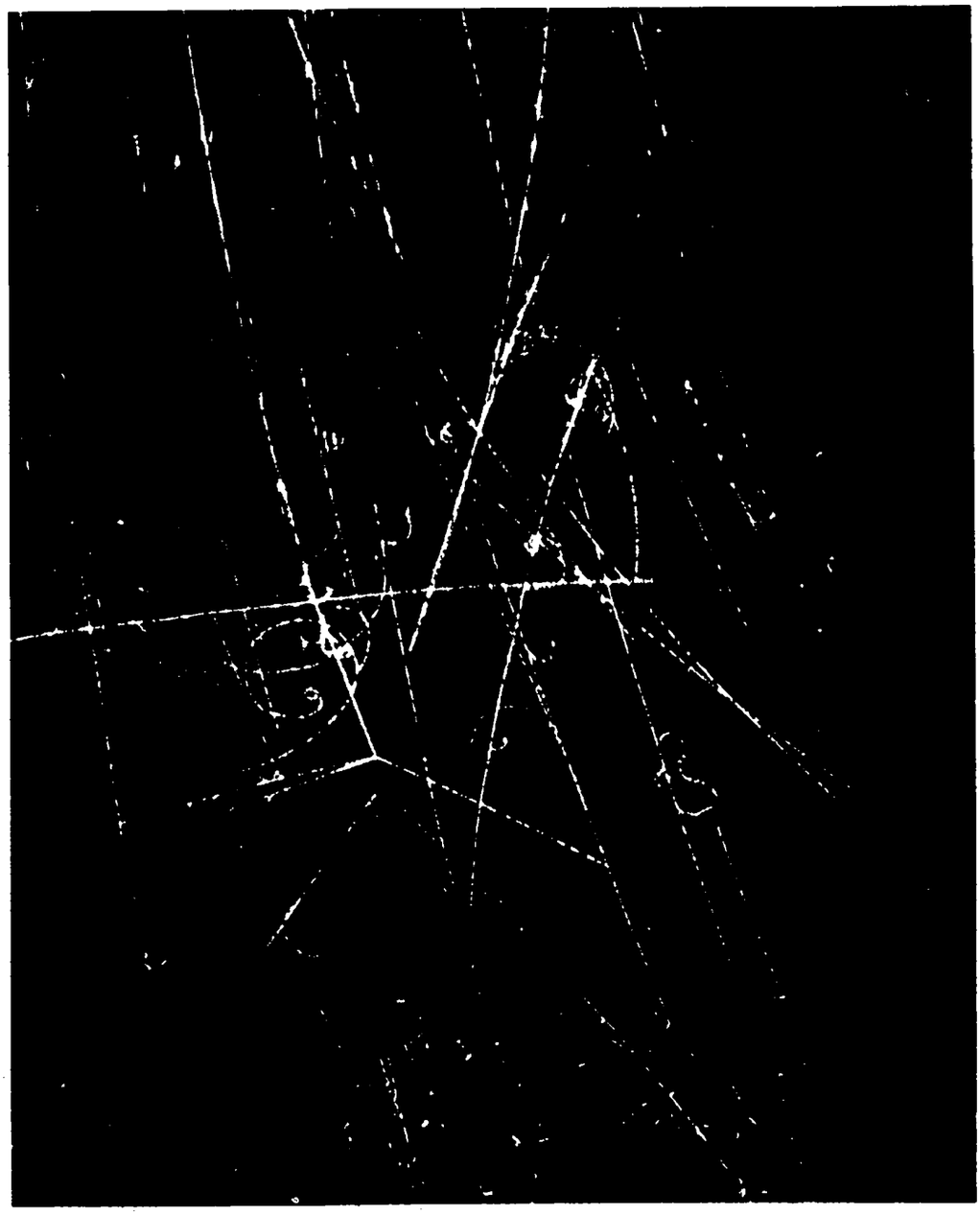

ZN-2203

Fig. 21. An antiproton enters at top left of picture and makes a heavy track until it annihilates into three charged prongs near center of picture. Directly below the annihilation is a $K^0 \longrightarrow \pi^+ + \pi^-$ event. Above and to the right of the annihilation is a Λ^0 with a projected opening angle near 0^o. Event number 28004.

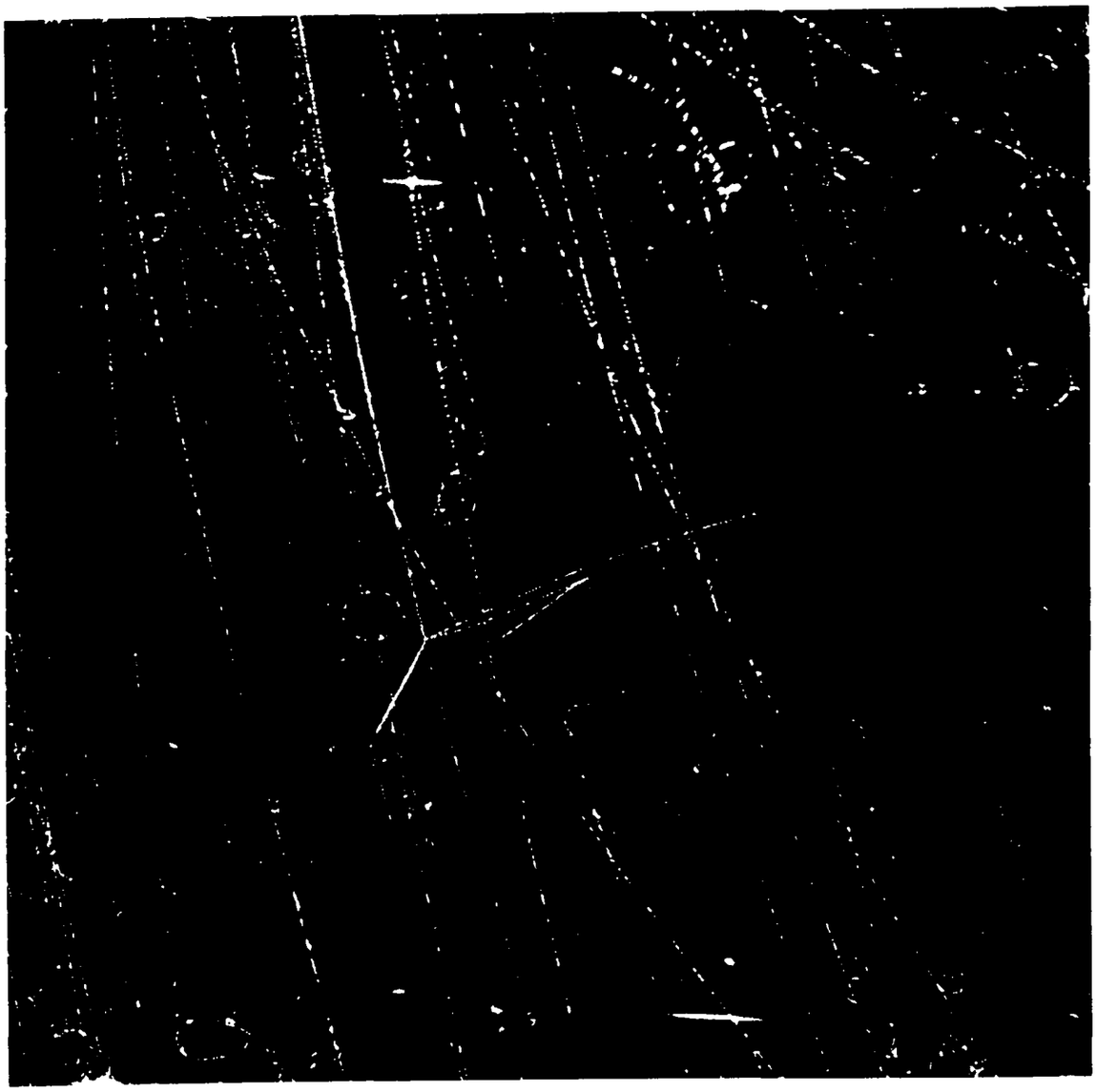

ZN-2202

Fig. 22. An antiproton enters at top left of picture and makes a heavy track until it annihilates near center of picture. The longer of the two prongs on the right may be seen to decay, sending a minimum-ionizing particle down and out of the bottom of the picture. This is a $K^+ \longrightarrow \pi^+ + \pi^0$ at rest. Event number 36046.

It should be pointed out that all strange particles (hyperons or K-mesons) associated with an annihilation event can be assumed to result, either directly or indirectly, from the initial $\bar{N}N$ creation of a K-meson pair during annihilation. Other methods of producing strange particles are ruled out by reasons discussed in the next paragraph.

The production of a pair of K mesons by an annihilation pion is ruled out because of the high threshold energy required. One must also consider the reaction $\pi + N \rightarrow K + Y$, which might be expected to occur as the result of the interaction of a pion created in an annihilation and one of the residual nucleons in a carbon nucleus.[1] Only about 2% of the pions created in an annihilation have sufficient energy to exceed the threshold for the case. Using a mean free path in nuclear matter of $\sim 2 \times 10^{-11}$ cm for the process, we arrive at the prediction that only about 1/2 an event should occur in all of our $\bar{p}$-C annihilations.

Hyperons can be made in carbon annihilations via an indirect process. The exothermic reaction $K + N \rightarrow \pi + Y$ can occur within the same carbon nucleus as annihilation. Hence annihilation-produced K^- or $\bar{K}^0$ mesons may be converted into Λ^0 or Σ hyperons. Figure 21 contains a Λ^0 which is presumably an example of this process.

The same reaction, $K + N \rightarrow \pi + Y$, when it occurs within the chamber but at some distance from the annihilation, is sufficient to verify the identification of a K^- meson.

In our selected group of 436 annihilations, we were able to identify twelve as producing strange particles, with a tentative identification for five others. These events are listed and very briefly described in Tables XIII, XIV, and XV. We believe that our scanning efficiency for $K_1^0 \rightarrow \pi^+ + \pi^-$ is practically 100%, since they decay within a few centimeters of the annihilation, a region which is subjected to closest inspection. Scanning efficiency for the charged mesons is not greater than 70%. This number is obtained by assuming all $K^\pm$ mesons with dip angle greater than 45° to be undetectable. Upon adopting this assumption we establish 45° dip angle as a cutoff and ignore possible charged K mesons that have steeper angles. This also assumes that all charged K mesons with dip angles within the accepted values are detectable. Above 150 Mev, this last assumption becomes risky, for the K ionization drops below twice minimum. If we compare our observed K energy spectrum (Fig. 23) and the spectrum predicted by Sandweiss for 2 K mesons accompanied by 2 pions (2 K mesons accompanied by at least 2 pions seems indicated by data in Table III),[54] we get good agreement in the ratio of K mesons above 150 Mev with respect to total number of K mesons. In summary, we feel uneasy about our ability to detect charged K mesons, especially above 150 Mev, but we are unable to devise a reliable estimate of efficiency.

Restricting ourselves to those twelve cases in which definite identification could be made, we find 4 K_1^0 (including event No. 32327), 7 K^+, 4 K^-, and 2 Λ^0. For the 4 K_1^0 observed we make a small correction for the 14% branching ratio mode, $K_1^0 \rightarrow \pi^0 + \pi^0$, which is unobserved. We then again correct for the long-lived K_2^0 decays, giving us a total of 9.3 K^0 mesons. Still another correction

should be made to the neutral K mesons to account for the $\bar{K}^0$ absorption or hyperon production in the same nucleus as annihilation occurs. Observation of 2 Λ^0 hyperons among the products of $\bar{p}$ annihilation in carbon indicates some 3 events (1/3 of the Λ^0 decay neutrally) in which either a K^- or a $\bar{K}^0$ meson has interacted.[55] We assume that 1.5 $\bar{K}^0$ and 1.5 K^- mesons have so interacted. This yields a total of 10.8 K^0 mesons.

Turning now to the charged K mesons, we apply our scanning correction to the 7 K^+ and 4 K^- to get 10 K^+ and 5.7 K^-. We also add 1.5 K^- for interaction in carbon nuclei for a total of 10 K^+, 7.2 K^-, or 17.2 charged K particles in all.

Adding together charged and neutral K mesons, we find 28 in 436 annihilations, which yields $3.2^{+1.0}_{-0.8}$ % of the annihilations giving $K\bar{K}$ pairs. The error stated is statistical and based on the 17 observed events. This result may be regarded as a lower limit. If we inspect the 17 events listed in Table XIII, we see 8 particles with strangeness = +1, 7 with S = -1, and 2 K_1^0, for which strangeness is undefined.

If we include the tentatively identified strange particles (Table XIV) in our calculations, then we obtain the result that 4.2 ± 0.9% of the annihilations produce $K\bar{K}$ pairs.

In view of the uncertainties in scanning, and recognizing that some of the tentatively identified K mesons are probably valid, we feel that a best estimate is that 4.0 ± 1.2% of all annihilations produce $K\bar{K}$ pairs.

In Fig. 23 we present the kinetic energy spectrum of all the K mesons observed.

Table XIII

Identified strange particles associated with antiproton annihilation

Event	Strange particle	Identification method	$\frac{t}{\tau}$ [a]	Kinetic energy at decay (Mev)	Kinetic energy at annih. [b] (Mev)
22758	K^+	Ionization determination over 14 cm of track	-	--	74
28004	K^0	Good fit to annihilation origin Good fit to decay kinematics	0.3	120	120
	Λ^0	Good fit to annihilation origin Good fit to decay kinematics	0.6	112	112
28432	$K^+_{\mu 2}$	Elastic K^+-p scatter Ionization decrease upon forward decay Decay fits kinematics for $K_{\mu 2}$	0.1	104	235
31375	K^-	A Λ^0 is produced by the star at end of track	-	0	33
	K^+	Ionization decrease upon forward decay of stopping particle. Kinematics uncertain but π -μ decay easily ruled out.	-	0	93
31395	K^+	Ionization determination over 11 cm of track	-	-	70
	K^-	A negative track of greater than minimum ionization makes a star of two pions with total visible energy 457 Mev. The two pions have momenta consistent with the production and subsequent decay of a hyperon.	-	0	26

(Continued)

Table XIII (continued)

Event	Strange particle	Identification method	$\frac{t}{\tau}$ [a]	Kinetic energy at decay (Mev)	Kinetic energy at annih. [b] (Mev)
31978	K_1^0	This is a neutral K which fits annihilation origin .	0.1	187	187
32327	$K^+_{\pi 2}$	Good fit to decay kinematics. The pion decays in the chamber.	0.05	237	267
	V^0	Good fit to annihilation origin. The tracks are too steep to make momentum determination. Could be either a Λ^0 or $\bar{K}^0$.	(1.8 cm)	-	-
32913	K^-	Track of greater than minimum ionization makes a star which produces well-verified Λ^0.	-	$0 \leq T \leq 94$	$30 \leq T \leq 100$
36046	$K^+_{\pi 2}$	The track fits stopping K. The decay at rest agrees with $K^+_{\pi 2}$ mode.	-	0	43
37270	K^-	Stopping negative particle has no charged products. A Λ^0 fits the ρ star.	-	0	46
44480	Λ^0	Good fit to annihilation point. Satisfactory fit to decay kinematics.	0.2	32	32
	K^+	Tentative, based on ionization in 11 cm of track	-	-	89
45753	K_1^0	A neutral K which fits annihilation. One of the pions scatters and decay kinematics are not completely verified.	1.0	205	205

[a] The quantity $\frac{t}{\tau}$ is the ratio of the life of the particular particle with respect to its mean life.

[b] Kinetic energy of a strange particle upon leaving the point of antiproton annihilation.

Table XIV

Tentatively identified strange particles

Event	Strange particle	Identification method	$\frac{t}{\tau}$	Kinetic energy at decay	Kinetic energy at annih.
13324	Σ^+	Ionization decrease upon backward decay Identification of π- μ-e decay product.	2.3	83	92
22305	K^+	Determination of ionization in 12 cm of track	-	-	67
23060	K^+	Determination of ionization in 17 cm of track.	-	-	127
33554	Λ^0	Good fit to annihilation origin. Measurement of momentum of the pion decay product is uncertain.	1.8	85	85
43349	K^+	Determination of ionization in 18 cm of track.	-	-	160

Table XV

Information about annihilations in which strange particles are created

Event	Strange particles	Annih. nucleus	Kinetic energy at annih. (Mev)	Other visible annih. products	Approx. missing energy (Mev)
Identified:					
22758	K^+	H	124	$2\pi^-$, $1\pi^+$, $1(\pi K)^-$[a], $1(p\pi)^+$	$0 < E < 400$
28004	$K^0 + \Lambda^0$	C	<50	$1\pi^-$, $1(p\pi)^+$, $2p^+$	$150 < E < 400$
28432	K^+	H	150	$1\pi^-$, $1\pi^+$, $1(\pi K)^-$	$0 < E < 300$
31375	$K^- + K^+$	C	71	$1\pi^+$, $2p^+$	500
31395	$K^- + K^+$	C	192	$1\pi^-$	600
31978	K_1^0	H	<50	$1\pi^-$, $2\pi^+$, $1(\Pi K)^-$	$0 < E < 300$
32327	$K^+ + V^0$	C	157	$1\pi^-$, $4p^+$	100
32913	K^-	H	<50	$1\pi^+$	1100
36046	K^+	C	0	$1(\pi K)^-$, $1(p\Pi)^+$	$500 < E < 1000$
37270	K^-	H	0	$1\pi^+$,	1100
44480	$K^+ + \Lambda^0$	C	0	$1\pi^+$, $1p^+$	800
45753	K_1^0	C	0	$1\pi^+$, $1(p\pi)^+$	$500 < E < 750$

(Continued)

Table XV (continued)

Event	Strange particles	Annih. nucleus	Kinetic energy at annih. (Mev)	Other visible annih. products	Approx. missing energy (Mev)
Tentative:					
13324	Σ^+	C	169	$3\pi^-$, $1\pi^+$, $2\,p^+$	500
22305	K^+	C	0	$2\pi^-$, $2\pi^+$, $1\,p^+$	100
23060	K^+	C	140	$1\pi^-$, $1\pi^+$, $1\,p^+$	800
33554	Λ^0	C	108	$2\pi^-$, $2\pi^+$, $3\,p^+$, $1\,(pK)^+$	$-500 < E < 0$
43349	K^+	H	50	$1\pi^-$	900

[a]The symbol $(\pi K)^-$ indicates that a steep negative track was observed, but particle identification was not possible.

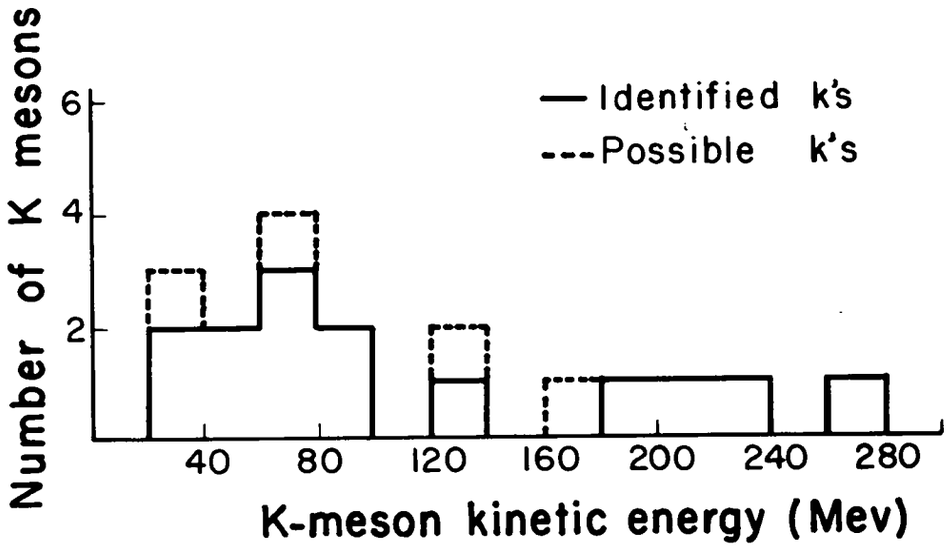

MU-17697

Fig. 23. A kinetic-energy histogram of K particles observed in association with antiproton annihilations. This plot is not corrected for charged-K scanning inefficiency, which is expected to be 100% below 100 Mev and probably decreases with increasing energy.

VI. ACKNOWLEDGMENTS

This work was undertaken upon the suggestion of Professor Emilio Segrè, to whom the author would like to express appreciation, not only for advice and encouragement on this particular task, but also for counsel throughout several years of graduate study.

During the past three years, the author has benefited greatly by association with Professor Owen Chamberlain, who has freely given of his time for advice and has also consistently demonstrated the methods and attitudes of the sound experimentalist.

The author's experiences have been enriched by association with Drs. Clyde Wiegand, Thomas Ypsilantis, Herbert Steiner, and William Fowler, all of whom contributed to the work described in this paper. This group is incomplete without the inclusion of Dr. Richard Lander, whose many contributions to the analysis and interpretation merit special acknowledgment.

The propane bubble chamber was built and operated under the direction of Professor Wilson Powell, who has been an interested participant. Mr. Larry Oswald held responsibility for much of the actual bubble-chamber operation.

To Mr. Howard White must go full credit for the development of the measuring methods and IBM programming for the analysis of the bubble-chamber events. Besides providing the apparatus, IBM programs, and staff, Mr. White accepted responsibility for the execution of the difficult task of measuring and computing.

The experimental success was due in no small part to the electronic selection apparatus built and operated by Mr. Tom Elioff and Dr. Clyde Wiegand. During the Bevatron run, Mr. Elioff contributed to a remarkable degree with his tireless effort.

The long task of scanning was considerably lightened by the cheerful cooperation of Professor Louis Gilly, who, during the course of his many hours of scanning, was first to recognize the antineutron annihilation.

Dr. Richard Weingart and Mr. William Johnson contributed generously of their time before, during, and after the experiment. The actual Bevatron run was carried out with the assistance of many

people, among whom are Dr. Janice Button and Messers James Foote, Joseph T. Lach, Rudolph R. Larsen, and Ernest Rogers.

The cooperation of the bevatron operating crew and staff, under the direction of Dr. Edward J. Lofgren, is appreciated.

Finally, I wish to thank Mrs. Alice Furth for her expert typing of most of the text and tables.

This work was done under the auspices of the U. S. Atomic Energy Commission.

VII. APPENDIXES

Appendix I. Choice of Target Material

An optical-model study of antiproton production by protons on complex nuclei has been made by R. Weingart.[56] He determined yield for optimum target length of various target materials. Optimum target length depends on the total inelastic scattering both of the incident proton in the target and the produced antiproton in the target, and is about 2/3 of the mean free path of the incident proton. Because little is known of antiproton production, an effective proton-nucleon cross section is defined for production inside the nucleus and is assumed independent of A. Attenuation of beam protons in the nucleus and antiproton annihilation in the nucleus of production are also treated through the use of the individual-nucleon cross section. For the nuclear density, a Fermi distribution consistent with the Stanford experiments is chosen. An effective production cross section for the nucleus, σ_{prod}, is then obtained by integrating over the path length in the nucleus. The results are shown in Fig. 24. All calculations were performed for an incident proton energy of 6.1 Bev and production of 440-Mev antiprotons. In Fig. 25, Weingart's results are shown with yield of antiprotons for optimum target length plotted against atomic weight, A. The results indicate an advantage in the use of materials of low A, and for this reason a beryllium target $\frac{1}{2}$ by $\frac{1}{2}$ by 6 in. long was chosen. This choice gives about 90% of the production by a Be target of 10 in., which is the optimum length.

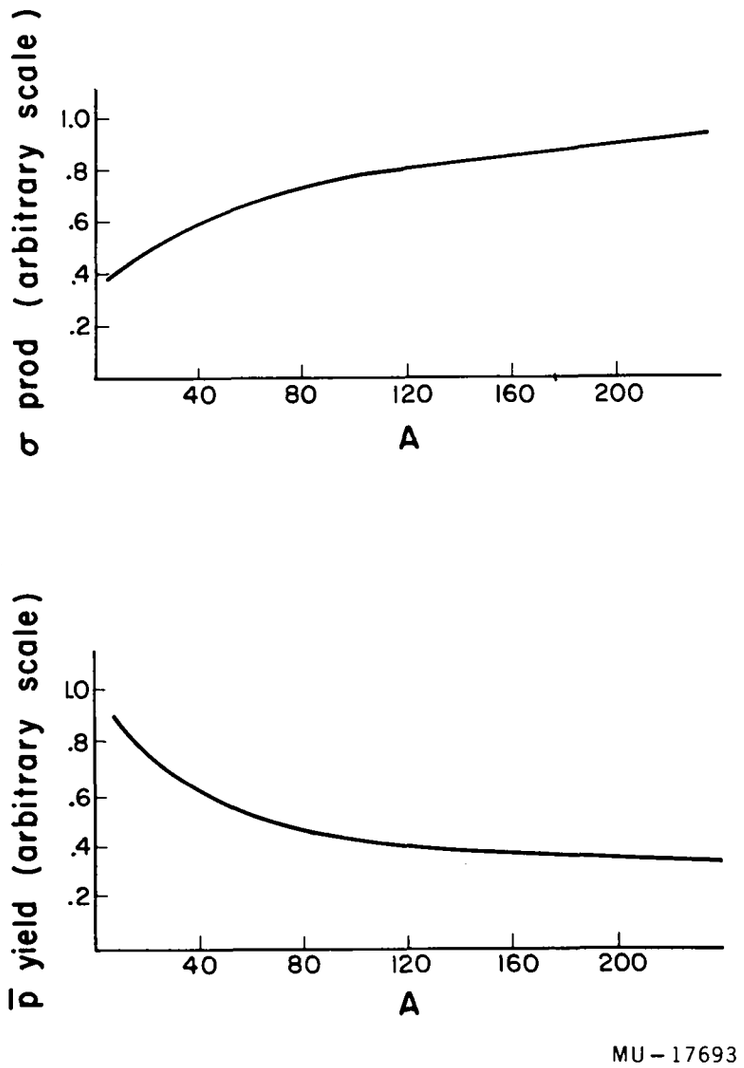

Fig. 24. Production per nucleus of 440-Mev antiprotons by 6.1-Bev protons vs. mass number (Reference 55).

Fig. 25. Yield at optimum target thickness of 440-Mev antiprotons produced by 6.1-Bev protons vs. mass number.

Appendix II. Choice of Absorber Material

In our separation system, it is essential to have a different change in momentum for antiprotons and pions that pass through a certain thickness of absorber. The antiprotons and pions enter the absorber with the same momenta, and we wish them to emerge with as different momenta as possible. We have a choice of the material and thickness of the absorber. For a given momentum loss of the antiprotons, the momentum loss of the pion is hardly affected by the material employed as absorber, as can be easily shown from the usual dp/dx relationship.

The choice of absorber material is thus determined by the desire to minimize the loss of antiprotons. Loss of antiprotons is primarily due to nuclear interaction and multiple coulomb scattering in the absorber. Once we fix the antiproton momentum change, a figure of merit, F, may be devised which is merely the product $F = RT$, where T is the antiproton transmission considering only multiple coulomb scattering, and R is the antiproton transmission considering only the annihilation and nuclear scattering cross section. In our beam setup, the absorber was followed by a strong-focusing magnet whose aperture formed an effective cutoff for scattered antiprotons. Then we can define:

$$T = 1 - \exp\left(-\frac{\theta^2}{\theta^2_{rms}}\right),$$

where θ is the half-angle subtended by the 8-in. quadrupole-focusing magnet following the absorber and θ_{rms} is the mean square angle for multiple scattering. The factor R is given by

$$R = \exp\left(-\frac{t}{\lambda}\right),$$

where λ is the antiproton mean free path for annihilation and scattering to angles greater than θ. Figure 26 shows F vs. A for a representative case, namely P_i = 800 Mev/c, $P_f(\bar{p})$ = 700 Mev/c, and θ = 0.033. Values of λ used in the calculation corresponded to $2\sigma_r$ as reported by Agnew et al.[4]

Low-Z elements being strongly favored, beryllium was selected as the most practical absorber.

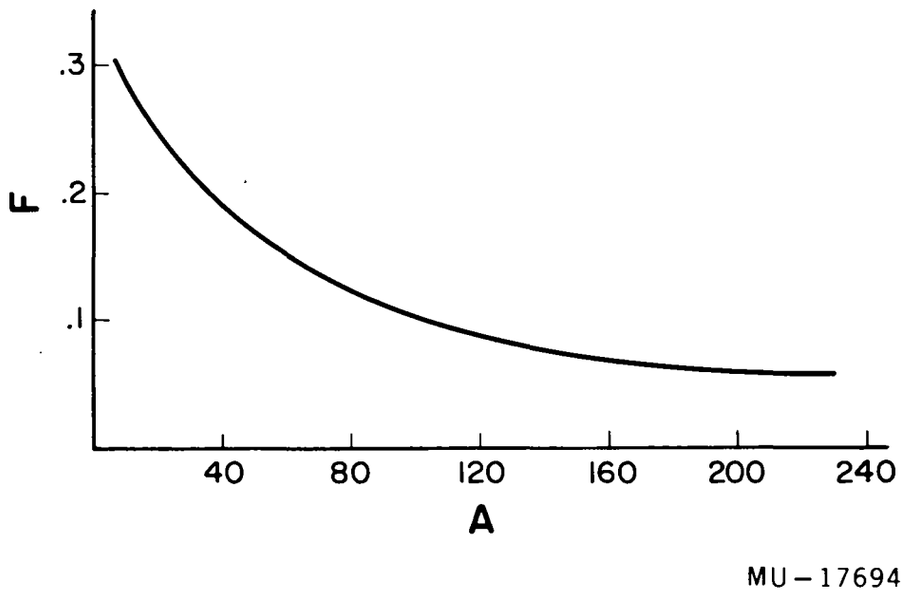

Fig. 26. The fractional transmission, F, of antiprotons through an absorber vs. the atomic weight, A, of the absorber. Antiproton momentum loss is the same for all values of A.

Appendix III. Pair Production in Propane above 25 Mev

The mean free path for pair production is a function of the energy of the photon. The theory has been worked out by Bethe and Heitler.[57] The theory is difficult to apply quantitatively for photon energies between 25 and 400 Mev in propane.

At the energies under consideration, photon attenuation is effectively due to the sum of Compton scattering and pair production. The Compton effect is accurately known theoretically. Thus the most reliable method of obtaining the mean free path for pair production, which is presented in Fig. 27, is to find first its reciprocal by subtracting the Compton-effect mass-absorption coefficient from the measured total mass-absorption coefficient. Data on total photon absorption has been tabulated.[58] The mass-absorption coefficient for Compton scattering is obtained from:

$$\tau_{Comp}(cm^2/g) = 0.2003 \frac{2Z}{A} \frac{3}{8} \frac{m_e c^2}{W_\gamma} \left(\ln \frac{2W_\gamma}{m_e c^2} + \frac{1}{2}\right),$$

where Z and A are the atomic number and atomic weight, and W_γ is the energy of the photon.

It should be pointed out that values of the mean free path for pair production plotted in Fig. 27 actually include triplet production. Triplet and pair production are lumped together as pair production because the recoil electron in triplet production is rarely (much less than 1% of the time) detectable in propane; i.e., the two processes are indistinguishable.

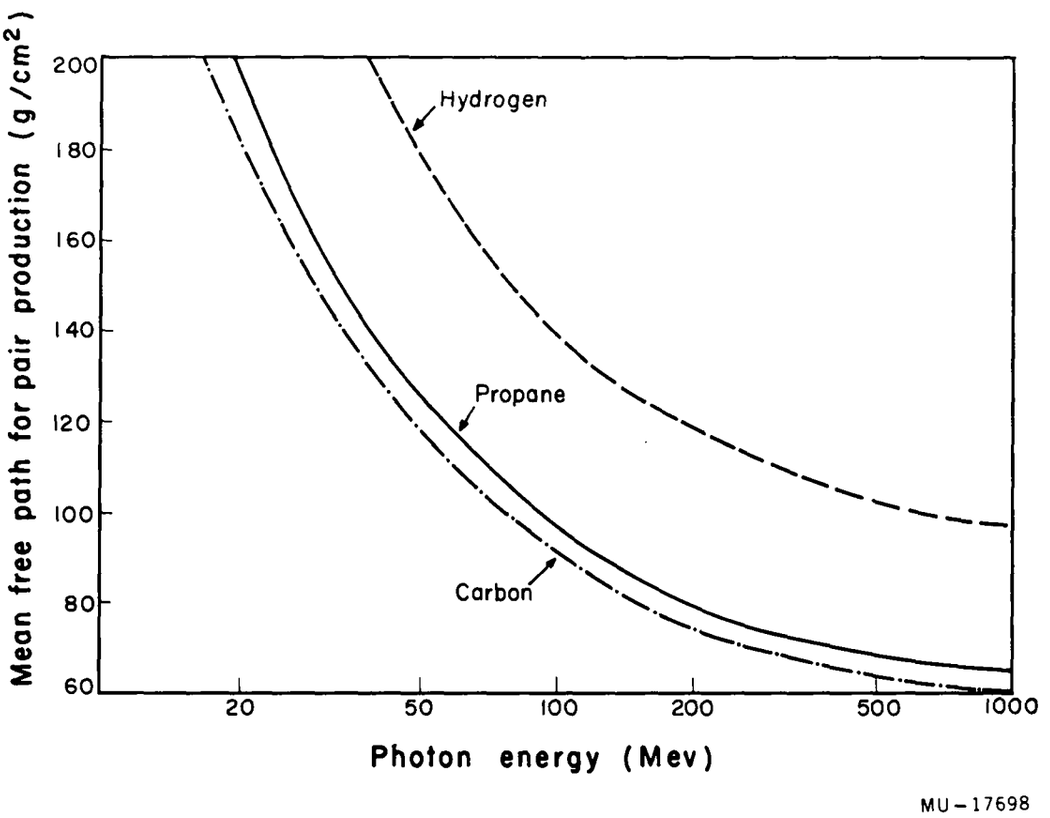

Fig. 27. A plot of mean free path for pair production in propane as a function of photon energy from 20 Mev to 1 Bev.

REFERENCES AND FOOTNOTES

1. Chamberlain, Segrè, Wiegand, and Ypsilantis, Phys. Rev. 100, 947 (1955).
2. Chamberlain, Keller, Segrè, Steiner, Wiegand, and Ypsilantis, Phys. Rev. 102, 1637 (1956).
3. Cork, Lambertson, Piccioni, and Wenzel, Phys. Rev. 107, 248 (1957).
4. Agnew, Chamberlain, Keller, Mermod, Rogers, Steiner, and Wiegand, Phys. Rev. 108, 1545 (1957).
5. Chamberlain, Keller, Mermod, Segrè, Steiner, and Ypsilantis, Phys. Rev. 108, 1553 (1957).
6. Button, Elioff, Segrè, Steiner, Weingart, Wiegand, and Ypsilantis, Phys. Rev. 108, 1557 (1957).
7. Barkas, Birge, Chupp, Ekspong, G. Goldhaber, S. Goldhaber, Heckman, Perkins, Sandweiss, Segrè, Smith, Stork, Van Rossum, and Amaldi, Baroni, Castagnoli, Franzinetti, and Manfredini, Phys. Rev. 105, 1037 (1957).
8. Chamberlain, Goldhaber, Jauneau, Kalogeropoulos, Segrè, and Silberberg, Phys. Rev. 113, 1615 (1959).
9. Coombes, Cork, Galbraith, Lambertson, and Wenzel, Phys. Rev. 112, 1303 (1958).
10. Horwitz, Miller, Murray, and Tripp, Phys. Rev. (in press).
11. E. Segrè, Annual Rev. Nuclear Sci. 8, 127 (1958).
12. J. Ball and G. Chew, Phys. Rev. 109, 1385 (1958).
13. S. Gartenhaus, Phys. Rev. 107, 291 (1957).
14. P. Signell and R. Marshak, Phys. Rev. 109, 1229 (1958).
15. Baroni, Belletini, Castagnoli, Ferro-Luzzi, and Manfredini, Nuovo cimento 12 564 (1959).
16. Z. Koba, and G. Takeda, Progr. Theoret. Physics 19, 269 (1958).
17. Cork, Lambertson, Piccioni, and Wenzel, Phys. Rev. 104, 1193 (1956).
18. Hans Bethe, Ann Physik 5, 325 (1930) and H. Bethe and J. Ashkin, Experimental Nuclear Physics, Vol. I, E. Segrè, editor, (John Wiley and Sons, New York, 1953).

19. Joseph J. Murray, A Coaxial Static-Electromagnetic Velocity Spectrometer for High-Energy Particles, UCRL-3492 May 7, 1957
20. Powell, Fowler, and Oswald, Rev. Sci. Instr. 29, 874 (1958).
21. See Appendix I.
22. See Appendix II.
23. J. R. Fulco, Phys. Rev. 110, 784 (1958).
24. J. S. Ball, and J. R. Fulco, Phys. Rev. 113,647 (1959).
25. The results of several groups have been compiled by Baroni et al. (see reference 15).
26. F. Bjorklund and S. Fernbach, University of California Radiation Laboratory, Livermore, and J. Fulco, University of California Radiation Laboratory, Berkeley, private communication.
27. The pair conversion of π^0-decay photons in the propane bubble chamber is discussed at some length in Section VA.
28. This is true for 33 two-prong annihilations in the hydrogen bubble chamber (Donald H. Miller, University of California Radiation Laboratory, Berkeley, private communication) and for 54 cases reported in this paper.
29. H. Bethe, and J. Hamilton, Nuovo cimento 4, 1 (1956).
30. Antiproton Collaboration Experiment, Phys. Rev. 105, 1037 (1956), gives I-spin arguments that favor a low π^0 multiplicity in ρ stars.
31. On the assumption that the carbon and hydrogen cross sections are equal, we get $\sigma \leq 11$ mb. The possibility of equal cross sections is suggested by Button et al. in reference 2.
32. I am indebted to Professor Robert Serber of Columbia University for some very useful comments on the $\bar{p}$-capture process at rest in propane. The capture of negative particles stopping in chemical compounds is discussed by E. Fermi and E. Teller, Phys. Rev. 72, 399 (1947).
33. H. Bethe and J. Hamilton, Nuovo cimento 4, 1 (1956).
34. Day, Snow, and Sucher, Phys. Rev. Lett. 3, 61 (1959).

35. Panofsky, Aamodt, and Hadley, Phys. Rev. 81, 565 (1951).
36. W. B. Riesenfeld and K. M. Watson, Phys. Rev. 102, 1157 (1956).
37. F. Bjorklund and S. Fernbach, Lawrence Radiation Laboratory, University of California, Livermore, California (private communication).
38. It would clearly be incorrect to report on only this 65%, because they are not representative of all the annihilations. The undetermined prongs occur most frequently in stars of high multiplicity.
39. No correction is necessary for center-of-mass motion in the case of annihilation at rest. This region is a little more than half the center-of-mass solid angle for in-flight annihilations.
40. See Appendix III.
41. Orear, Harris, and Taylor, Bull. Am. Phys. Soc. 2, 6 (1957).
42. To justify this, we inquire how much energy is carried off by unobserved neutrons. Energetic neutrons from carbon stars must be expected to have about the same energy distribution as energetic protons, which we can observe. Even if all 40 $\bar{p}p$ stars have one energetic neutron, which is a very pessimistic estimate, the average energy per hydrogen-like annihilation available to pions is only reduced by 1.5%.
43. The error in this quantity indicates the influence of statistical fluctuation on the mean multiplicity. This error is not intended to characterize the shape of the charged-pion frequency distribution.
44. G. Sudarshan, Phys. Rev. 103, 777 (1956).
45. S. Frautschi, Research Institute for Fundamental Physics, Kyoto University, Kyoto, Japan, private communication.
46. The scattering is inelastic because it occurs in the presence of the nucleus. Process 2 is intended to be the inside-the-nucleus version of $\pi + N \rightarrow \pi + N$.

47. Another interaction that will be ignored in this paper is the production of pions by pions, which becomes important at energies above 500 Mev.

48. S. J. Lindenbaum, Ann. Rev. Nuclear Sci. 7, 330 (1957).

49. Frank, Gammel, and Watson, Phys. Rev. 101, 891 (1956).

50. J. R. Fulco, Phys. Rev. 114, 374 (1959).

51. We obtain this number by assuming multiplicity varies as $\sqrt{\frac{E}{E_0}}$. This value happens to agree very well with our results, but our statistics do not warrant any conclusions about change in pion multiplicity vs total energy available.

52. Amaldi, Baroni, Bellettini, Castagnoli, Ferro-Luzzi, and Manfredini, Istituto di Fisica Dell'Universita, Roma, Italy and Istituto Nazionale di Fisica Nucleare, Sezione di Roma, Italy, private communication.

53. R. Gatto, Nuovo cimento, 3, 468 (1956).

54. J. Sandweiss, On the Spin of K Mesons from the Analysis of Antiproton Annihilations in Nuclear Emulsions (Thesis), UCRL-3577, October 31, 1956.

55. This is not in disagreement with what is expected for about 10 K^- and $\overline{K}^0$ produced in carbon.

56. R. Weingart, Lawrence Radiation Laboratory, University of California, Livermore, private communication.

57. H. Bethe and W. Heitler, Proc. Roy. Soc. (London) A146, 83 (1934). Other comment will be found in Bruno Rossi, High-Energy Particles (Prentice-Hall, New York, 1952), and J. Ashkin and H. Bethe in Experimental Nuclear Physics, Vol. I, E. Segrè, editor (John Wiley and Sons, New York, 1953).

58. J. H. Atkinson, Jr. and B. H. Willis, High-Energy Particle Data, Vol. II, UCRL-2426 Rev, June 1957.